AD-A156 912 FEEDBACK STABILIZATION OF OPTICAL INTERFEROMETER(U) AIR FORCE INST OF TECH WRIGHT-PATTERSON AFB OH R H NAKAT FEB 85 AFIT/CI/NR-85-41T 1/1

UNCLASSIFIED F/G 20/6 NL

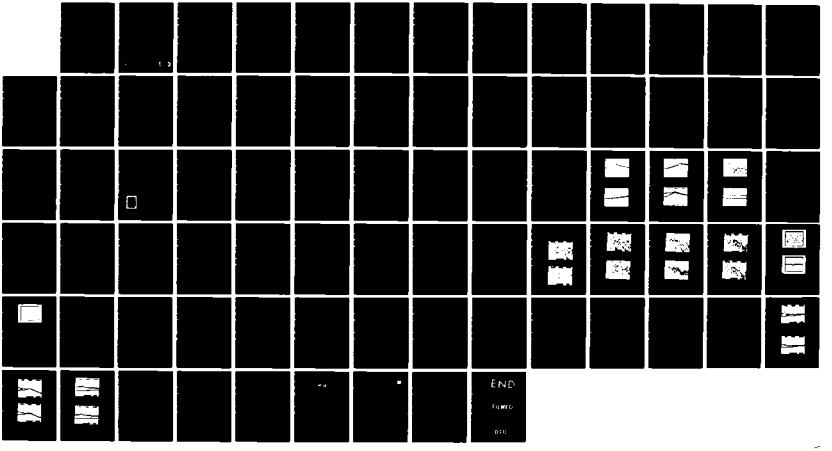

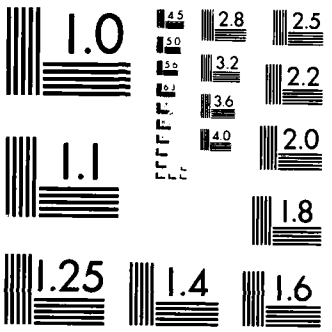

FEEDBACK STABILIZATION OF OPTICAL INTERFEROMETERS

by

1 Lt Robert Haruo Nakata, U.S. Air Force

Submitted to the Department of Electrical Engineering and Computer Science at the Massachusetts Institute of Technology on February 22, 1985 in partial fulfillment of the requirements for the degree of Master of Science in Electrical Engineering

ABSTRACT

An experimental study was carried out on the performance of a feedback stabilization scheme for optical interferometers. Optical interferometers are susceptible to acoustic noise which translates into path length fluctuations in the interferometer arms. These fluctuations induce phase noise, resulting in amplitude fluctuations on the interferometer output.

The experiment was performed on a Mach-Zehnder homodyne interferometer where a RMS noise reduction of 23 dB was observed. The stabilization scheme has application to other interferometer configurations. In the future, it will be applied to stabilize cavities used in the squeezed state generation of light.

Thesis Supervisor: Dr. Prem Kumar
Title: Staff Scientist, Research Laboratory of Electronics

70 pages.

UNCLASS

SECURITY CLASSIFICATION OF THIS PAGE *(When Data Entered)*

REPORT DOCUMENTATION PAGE		READ INSTRUCTIONS BEFORE COMPLETING FORM
1. REPORT NUMBER AFIT/CI/NR 85-41T	2. GOVT ACCESSION NO. AD-A156 912	3. RECIPIENT'S CATALOG NUMBER
4. TITLE *(and Subtitle)* Feedback Stabilization Of Optical Interferometers		5. TYPE OF REPORT & PERIOD COVERED THESIS/DISSERTATION
		6. PERFORMING ORG. REPORT NUMBER
7. AUTHOR(s) Robert Haruo Nakata		8. CONTRACT OR GRANT NUMBER(s)
9. PERFORMING ORGANIZATION NAME AND ADDRESS AFIT STUDENT AT: Massachusetts Institute of Technology		10. PROGRAM ELEMENT, PROJECT, TASK AREA & WORK UNIT NUMBERS
11. CONTROLLING OFFICE NAME AND ADDRESS AFIT/NR WPAFB OH 45433		12. REPORT DATE February 1985
		13. NUMBER OF PAGES 70
14. MONITORING AGENCY NAME & ADDRESS*(if different from Controlling Office)*		15. SECURITY CLASS. *(of this report)* UNCLASS
		15a. DECLASSIFICATION/DOWNGRADING SCHEDULE

16. DISTRIBUTION STATEMENT *(of this Report)*

APPROVED FOR PUBLIC RELEASE; DISTRIBUTION UNLIMITED

17. DISTRIBUTION STATEMENT *(of the abstract entered in Block 20, if different from Report)*

18. SUPPLEMENTARY NOTES

APPROVED FOR PUBLIC RELEASE: IAW AFR 190-1

14 March

Lynn E. Wolaver

LYNN E. WOLAVER
Dean for Research and
Professional Development
AFIT, Wright-Patterson AFB OH

19. KEY WORDS *(Continue on reverse side if necessary and identify by block number)*

20. ABSTRACT *(Continue on reverse side if necessary and identify by block number)*

ATTACHED

DD FORM 1 JAN 73 1473 EDITION OF 1 NOV 65 IS OBSOLETE

UNCLASS

SECURITY CLASSIFICATION OF THIS PAGE *(When Data Entered)*

FEEDBACK STABILIZATION OF OPTICAL INTERFEROMETERS

by

1 Lt Robert Haruo Nakata, U.S. Air Force

Submitted to the Department of Electrical Engineering and Computer Science at the Massachusetts Institute of Technology on February 22, 1985 in partial fulfillment of the requirements for the degree of Master of Science in Electrical Engineering

ABSTRACT

An experimental study was carried out on the performance of a feedback stabilization scheme for optical interferometers. Optical interferometers are susceptible to acoustic noise which translates into path length fluctuations in the interferometer arms. These fluctuations induce phase noise, resulting in amplitude fluctuations on the interferometer output.

The experiment was performed on a Mach-Zehnder homodyne interferometer where a RMS noise reduction of 23 dB was observed. The stabilization scheme has application to other interferometer configurations. In the future, it will be applied to stabilize cavities used in the squeezed state generation of light.

Thesis Supervisor: Dr. Prem Kumar
Title: Staff Scientist, Research Laboratory of Electronics

70 pages.

ACKNOWLEDGEMENTS

I would like to thank my thesis supervisor, Dr. Prem Kumar for his guidance and assistance during the course of research on this thesis. Discussions with my colleagues, Mari Maeda and Seng-Tiong Ho were also very helpful. I am greatly indebted to my wife for her moral support and for her assistance with the typing and illustrations. I also thank the U.S. Air Force for sponsoring my graduate education.

BIOGRAPHICAL NOTE

The author was born on March 7, 1959 at Ashiya Air Force Base, Japan. He attended grammar school on various military installations throughout Japan and Okinawa and later moved to Hawaii where he completed his high school education. Upon graduation from MIT in 1981, he was commissioned as an officer in the U.S. Air Force and worked as a project engineer on several Department of Defense programs. He returned to MIT in February, 1984 and expects to complete his graduate studies in February, 1985.

TABLE OF CONTENTS

CHAPTER 1

INTRODUCTION

The objective of this thesis is to stabilize an optical interferometer used in an optical homodyne system. A Mach-Zehnder interferometer optical homodyne system is shown in Fig. 1.1. This system was used to verify the laser excess noise reduction capability with dual detection [1]. In this configuration, a single dye laser beam is split into a signal beam, E_S, and a local oscillator (LO) beam, E_L. The signal beam is field modulated by an electro-optic modulator (EOM) driven by a radio frequency (RF) source. When the signal beam is recombined with the LO beam at the output beam splitter (BS), the resultant intensity at detector 1 is given by (the details are presented in Chapter 6)

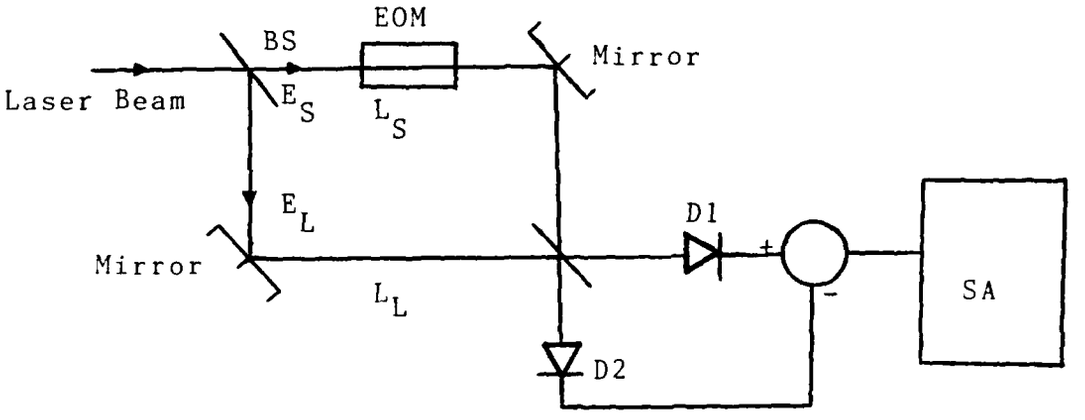

Fig. 1.1 Mach-Zehnder interferometer configured as a dual detection optical homodyne receiver.

$$P_1 = Y_o[\, E_S^2 \sin^2 \omega_m t + E_L^2 + 2E_S E_L \cos[k(L_L - L_S)] \sin \omega_m t] \quad (1.1)$$

where ω_m = modulation frequency = $2\pi f_m$

L_S = signal arm path length

L_L = LO arm path length

Y_o = free space admittance

and E_S and E_L are assumed real.

The detector current is proportional to P_1 whose spectrum, monitored at the spectrum analyzer (SA), shows two peaks, one at frequency ω_m/π contributed by the first term in Eq. (1.1) and the second at frequency $\omega_m/2\pi$ contributed by the last term. It was observed that the amplitude of the ω_m/π peak remained stable whereas the $\omega_m/2\pi$ peak fluctuated randomly [1]. The reason for this behavior is due to the $\cos[k(L_L - L_S)]$ factor in the last term of Eq. (1.1) as explained below.

A noisy environment causes the path length of each interferometer arm to fluctuate as the mirror positions fluctuate. Optical interferometers are, in general, susceptible to mechanical and acoustic vibrations because the phase of the field propagating in each arm is path length dependent. This is evident in the last term of Eq. (1.1). Thus, path length variations due to these vibrations manifest themselves as intensity fluctuations on the interferometer output. The purpose of this thesis is to repeat the above experiment with a stabilized Mach-Zehnder interferometer

where the effect of these vibrations is actively compensated.

Fluctuations on the interferometer output also arise from the laser source. Laser frequency drift, excess noise and polarization noise must be eliminated if their contribution is significant. These effects are analyzed in Section 2 of Chapter 2.

The goal of the stabilization scheme is to achieve the quantum limit of photodetection. For this purpose a low noise, wideband transimpedance amplifier is designed and constructed. Photodetection noises are discussed in Chapter 3. Noise analysis and experimental performance of the transimpedance amplifier are presented in Chapter 4.

The interferometer stabilization is achieved by a servo feedback loop that correlates the path lengths in the two arms of the interferometer. An error signal is derived from the output fluctuations and applied to a piezo electric transducer (PZT) which drives a mirror in one of the arms of the interferometer, cancelling the path length variation. An alternative method of compensating for the path length variation is to phase modulate one of the arms of the interferometer with the EOM driven by the error signal. The effect is to cancel the phase jitter due to the noise by equalizing the phase in the two arms. The details of these optical feedback stabilization schemes are discussed in Chapter 5.

Finally, the experimental results of a homodyne

experiment are presented in Chapter 6. The data for the "noisy" interferometer is compared with that of the stabilized interferometer. It is demonstrated that the modulation signal fluctuations are reduced to the quantum limit when the interferometer is stabilized.

CHAPTER 2

SOURCES OF INTERFEROMETER OUTPUT FLUCTUATIONS

2.1 Interferometer Phase Sensitivity

The output of an optical interferometer, such as a Mach-Zehnder interferometer, will fluctuate due to random fluctuations in the lengths of the two arms of the interferometer. This is because the interferometer output is sensitive to the phase of the fields in each arm. Similar phase sensitivity also occurs for other types of interferometers such as the Michelson or the Fabry-Perot. The analysis to follow is for a Mach-Zehnder homodyne interferometer. Figure 2.1 shows a Mach-Zehnder interferometer where the subscripts "S" and "L" denote the signal and local oscillator fields.

The fields at the output of the input beam splitter are

$$\underline{E}_S = E_S \exp[j(\phi_S + \omega_S t)]$$

and

$$\underline{E}_L = E_L \exp[j(\phi_L + \omega_L t)] \qquad (2.1)$$

where $\omega_S = \omega_L$ for a homodyne system.

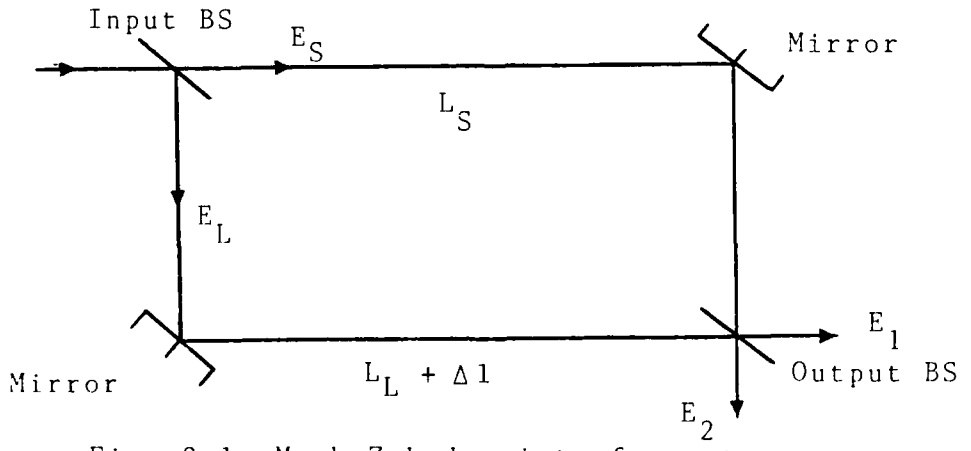

Fig. 2.1 Mach-Zehnder interferometer

Let L_S be the signal arm path length and $L_L + \Delta l$ be the LO arm path length. As will be seen later, it is the difference in the path lengths of the two arms that is of significance. Thus, we lump the fluctuations of both arms into a single term , Δl.

The fluctuation, Δl, can be modelled as a random process with a mean value which is added to the difference in the path lengths of the two arms and a variance which describes the extent of the mirror vibrations and other perturbations. The noise spectrum extends to several tens of KHz but is dominant at frequencies in the range from tens to hundreds of Hz. Assuming that the perturbation arises from a number of independent sources, $\Delta l(t)$ can be modelled as a Gaussian process.

The scattering matrix of a beam splitter is [2]

$$S = \begin{bmatrix} r & jt \\ jt & r \end{bmatrix} \tag{2.2}$$

where r is the reflection coefficient and t is the transmission coefficient. For a 50/50 beam splitter, the coefficients are $r = t = 1/\sqrt{2}$.

The interferometer output fields, E_1 and E_2 are obtained by the transformation

$$\begin{bmatrix} E_1 \\ E_2 \end{bmatrix} = \begin{bmatrix} r & jt \\ jt & r \end{bmatrix} \begin{bmatrix} \underline{E}_S \exp(-jkL_S) \\ \underline{E}_L \exp[-jk(L_L + 1) \end{bmatrix} \tag{2.3}$$

the amplifier is an ideal noiseless device.

The voltage noise, V_A, is primarily due to thermal noise associated with the channel resistance of a FET. It behaves as [6] (per unit bandwidth)

$$\langle V_A^2 \rangle = \delta 4kT/g_m \tag{4.5}$$

where g_m = forward transconductance

δ = .7 for Silicon, 1.1 for GaAs.

Noise in bipolar devices is due primarily to shot noise arising from the base and collector currents, I_b and I_c, respectively. These appear as [6] (per unit bandwidth)

$$\langle I_A^2 \rangle = 2eI_b \tag{4.6}$$

and $$\langle V_A^2 \rangle = 2(kT)^2/eI_c = 2(kT)_b^2/eI_b\beta \ , \tag{4.7}$$

where β = current gain.

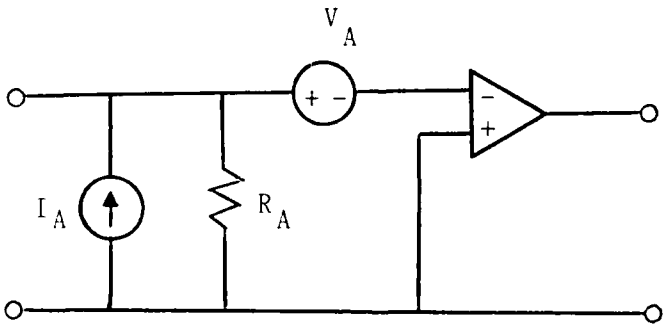

Fig. 4.2: Amplifier Noise Model.

The transfer function is found as follows:

Kirchoff's Current Law at the input node gives

$$I_s + \frac{V_o - V_{in}}{R_f} = \frac{V_{in}(j2\pi fRC + 1)}{R} \quad .$$

Since $V_o = -A\ V_{in}$, then

$$I_s + V_o(1/R_f + 1/AR_f) = -V_o(j2\pi fRC+1)/AR$$

or $$V_o = \frac{-I_s R_f}{(1 + 1/A + R_f/AR + j2\pi fR_f C/A)} \quad . \qquad (4.1)$$

Notice that when $A >> (1 + R_f/R)$

$$V_o = \frac{-I_s R_f}{1 + j2\pi fR_f C/A} \quad . \qquad (4.2)$$

There is a single pole at

$$f = A/2\pi R_f C \qquad (4.3)$$

which corresponds to the bandwidth of the transimpedance amplifier for a large open loop gain A. For $A >> 2\pi fR_f C$, the expression for V_o reduces to

$$V_o = -I_s R_f \quad . \qquad (4.4)$$

The amplifier functions as a current to voltage converter with a gain equal to the transimpedance R_f.

4.2 Noise Analysis

Amplifier Noise Sources

Amplifier noise manifests itself as thermal noise current due to the amplifier input resistance and as a voltage noise source. This is depicted in Fig. 4.2, where

CHAPTER 4

THE TRANSIMPEDANCE AMPLIFIER

A low noise amplifier is required to achieve the quantum limit of photodetection in the optical homodyne experiment. Since shot noise is proportional to the laser power, amplifier thermal noise must be minimized when the source is a low power laser. The amplifier thermal noise must be less than the detector shot noise to achieve the quantum limit.

The transimpedance amplifier yields both low noise and a large dynamic range without the need for equalization [3,4,5]. In this chapter, the transimpedance amplifier is analyzed for its noise performance. A prototype is built and experimental results verify the theoretical performance.

4.1 Op Amp as a Transimpedance Amplifier

An op amp configured as a transimpedance amplifier is shown in Fig. 4.1.

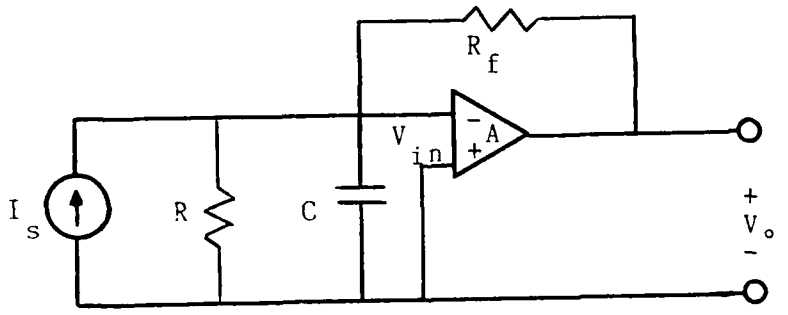

Fig. 4.1 Transimpedance Amplifier

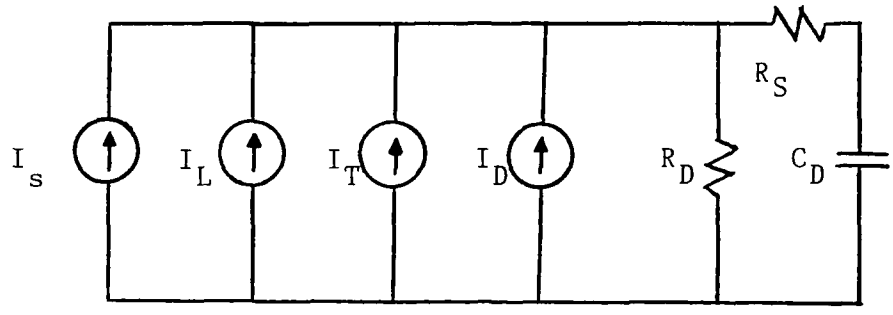

$I_s = Pe\eta/h\nu$ $\quad R_D$ = junction resistance

$\langle I_L^2 \rangle = 2eI_s$ $\quad R_S$ = series resistance

$\langle I_T^2 \rangle = 4kT/R_D$ $\quad C_D$ = junction capacitance

$\langle I_D^2 \rangle = 2eI_d$

Fig. 3.1 Photodiode Model

Thermal Noise

The junction resistance of a photodiode gives rise to thermal noise. Thermal noise is due to thermally excited random motion of free electrons in a conducting medium, such as a resistor.

The thermal noise mean square current spectral density (per unit bandwidth) is [2]

$$\langle I_T^2 \rangle = 4kT/R \qquad (3.2)$$

where k = Boltzman's constant, T = temperature of the resistor in degrees Kelvin and R = resistance.

Dark Current

Photodiode dark current is the current that is present when no light is incident on the detector. The dark current mean square current spectral density (per unit bandwidth) is [2]

$$\langle I_D^2 \rangle = 2eI_d, \qquad (3.3)$$

where I_d = dark current.

A photodiode can thus be modeled as shown in Fig. 3.1. The model will be used in the noise analysis of the detector/transimpedance amplifier discussed in Chapter 4.

CHAPTER 3

PHOTODETECTION NOISES

The goal of the stabilization scheme is to achieve the quantum limit of photodetection in the optical homodyne experiment. The objective of this section is to introduce the basic theory of photodetection and the noise associated with it. These noise sources will impose a limit on the "quietness" of the detector/amplifier to be discussed in Chapter 4. The origin and extent of shot noise, thermal noise and dark current noise is discussed below.

Shot Noise

Free electron-hole pairs are generated in a photodiode when light impinges upon the detector. By placing a reverse bias voltage across the photodiode, the charge carriers separate, producing a photocurrent.

The electron-hole generation process is statistical in nature and gives rise to a phenomenon known as shot noise. Shot noise results from the fluctuation of current around a mean value due to the discrete charge created during the photoabsorption process.

Shot noise sets an upper limit on a receiver's sensitivity. The shot noise mean square current spectral density (per unit bandwidth) is [2]

$$\langle I_L^2 \rangle = 2eI_s, \tag{3.1}$$

where $I_s = P\eta/h\nu$ as defined in Eq. (2.24).

slope which changes the transfer gain.

In summary, the sources of fluctuations are path length variations, refractive index variations, laser frequency drift, laser excess noise and laser polarization noise. The path length and refractive index variations are stabilized by applying negative feedback to the system. Laser frequency drift is not a problem when the detector response is less than the mode separation. Excess noise is minimized by dual detection subtraction. Finally, polarization noise is minimized by detecting a component that is polarized 45 degrees to both modes.

Next, we discuss photodetection noise sources which will constrain the minimum system noise.

expression of Eq. (2.7). The mean photocurrent generated in each detector is found from

$$I = Pe\eta/h\nu \tag{2.24}$$

where P = incident intensity, e = electron charge, h = Planck's constant and ν = laser frequency. For detector quantum efficiencies $\eta_1 = \eta_2 = \eta$, and for a 50/50 beam splitter, the mean photocurrents generated at each detector are

$$I_1 = (Y_o e\eta/2h\nu)[E_1(t)^2 + E_2(t)^2][1 + \cos[k(L_L - L_S + \Delta 1)]] \tag{2.25}$$

and

$$I_2 = (Y_o e\eta/2h\nu)[E_1(t)^2 + E_2(t)^2][1 - \cos[k(L_L - L_S + \Delta 1)]]. \tag{2.26}$$

Subtracting one from the other gives

$$I_1 - I_2 = (Y_o e\eta/h\nu)\,[E_1(t)^2 + E_2(t)^2][\cos[k(L_L - L_S + \Delta 1)]. \tag{2.27}$$

Therefore the DC terms are eliminated by subtraction.

When using a He-Ne laser to stabilize the interferometer with the dual detection subtraction signal, the polarizer placed at the output of the laser plays an important role. As the modes drift under the Doppler broadened gain curve, the individual mode intensities change but the intensity after the polarizer, which is proportional to $[E_1(t)^2 + E_2(t)^2]$, remains approximately constant. This ensures that the amplitude of the cosine factor in Eq. (2.27) remains constant, allowing the feedback stabilization to work. It will be shown in chapter 5 that the interferometer transfer gain is proportional to the slope of the cosine factor. Thus a fluctuation in amplitude will affect the

mode frequency. The difference in the arguments due to the different mode frequencies is negligible since the mode separation is much smaller (approximately 1 GHz) than the laser frequency (10^{14}). Thus, $k_1 \simeq k_2 = k$. Making this approximation, Eq. (2.20) becomes

$$P_1 = 2E_1(t)^2 + 2E_2(t)^2 + 2[E_1(t)^2 + E_2(t)^2]\cos(k\Delta 1)$$
$$= 2[E_1(t)^2 + E_2(t)^2][1 + \cos(k\Delta 1)] . \qquad (2.21)$$

To see how this case is stabilized, one can repeat the analysis for $L_L \neq L_S$, so that the difference term $L_L - L_S$ is introduced. This gives

$$P_1 = 2[E_1(t)^2 + E_2(t)^2][1 + \cos[k(L_L - L_S + \Delta 1)]. \qquad (2.22)$$

A similar derivation for P_2 gives

$$P_2 = 2[E_1(t)^2 + E_2(t)^2][1 - \cos[k(L_L - L_S + \Delta 1)]. \qquad (2.23)$$

As in the single mode analysis, the interferometer output is stabilized by feedback controlling $L_L - L_S$ so that the fluctuation is cancelled.

Laser Excess or Intensity Noise

Laser intensity fluctuations will also degrade the interferometer output signal. For the He-Ne laser intensity fluctuation, the $[E_1(t)^2 + E_2(t)^2]$ factor of Eqs. (2.22) and (2.23) will change causing an erroneous feedback signal to be applied. A dual detector configuration can alleviate this problem as shown below.

The interferometer output intensities are found from substituting Eqs. (2.22) and (2.23) into the intensity

yields

$$P_1 = |E_1(t)[1+\exp(-jk_1\Delta 1)] + E_2(t)\exp[j(\omega_2-\omega_1)t+j(k_1-k_2)L + j(\phi_2-\phi_1)][1+\exp(-jk_2\Delta 1)]|^2. \quad (2.16)$$

Evaluating the modulus gives

$$P_1 = E_1(t)^2[2+2\cos(k_1\Delta 1)]+E_2(t)^2[2+2\cos(k_2\Delta 1)] + 2E_1(t)E_2(t)\mathrm{Re}[\exp(j(\omega_2-\omega_1)t+j(k_1-k_2)L+j(\phi_2-\phi_1)) (1+\exp(-jk_2\Delta 1)(1+\exp(jk_1\Delta 1)]. \quad (2.17)$$

To simplify the expression, let the factor in brackets of the rightmost term be

$$[\ ] = \exp[j(\omega_2-\omega_1)t]A(t)\exp[j\Phi(t)]. \quad (2.18)$$

Equations (2.17) and (2.18) then give

$$P_1 = E_1(t)^2[2+2\cos(k_1\Delta 1)]+E_2(t)^2[2+2\cos(k_2\ \Delta 1)] + 2E_1(t)E_2(t)A(t)\cos[(\omega_2-\omega_1)t+\Phi(t)]. \quad (2.19)$$

The quantities $A(t)$, $\Phi(t)$, $E_1(t)$ and $E_2(t)$ fluctuate at acoustic frequencies. This is because the Fabry Perot resonator, which forms the cavity for the He-Ne laser, is susceptible to the same noises as the Mach Zehnder interferometer that we are trying to stabilize. Therefore the amplitude factor, $E_1(t)E_2(t)A(t)$, is a slowly varying envelope function for the second term in Eq. (2.19). Note that if $\omega_2-\omega_1$ is much greater than the frequency response of the detectors, equation (2.19) reduces to

$$P_1 = 2E_1(t)^2+2E_2(t)^2+2[E_1(t)^2\cos(k_1\Delta 1)+E_2(t)^2\cos(k_2\Delta 1)] \quad (2.20)$$

Unlike Eq. (2.8), for the case of a two mode laser the interferometer has a transfer function that is the sum of two cosines whose arguments are proportional to the respective

The following analysis shows that if the detector/amplifier frequency response is less than the mode separation, the effect of the frequency drift is not seen.

Let the laser output field be characterized by

$$\underline{\bar{E}}_o = \hat{x}2\underline{E}_1 + \hat{y}2\underline{E}_2 \tag{2.11}$$

where $\underline{E}_1$ and $\underline{E}_2$ are complex time varying fields associated with each polarization component.

It is appropropriate to mention here that an input polarizer preceding the input beam splitter is used while employing the He-Ne as the laser source. It is oriented so that its axis is 45 degrees from the polarization direction of each mode. Doing so ensures that light of a single polarization enters the interferometer and that the intensity stays relatively constant as the modes drift through the Doppler profile. The role of the polarizer is discussed in detail under excess noise.

We assume

$$\underline{E}_1 = E_1(t)\exp(j\phi_1 + j\omega_1 t) = \underline{E}_1' \exp(j\omega_1 t) \tag{2.12}$$

$$\underline{E}_2 = E_2(t)\exp(j\phi_2 + j\omega_2 t) = \underline{E}_2' \exp(j\omega_2 t) \tag{2.13}$$

For the interferometer configuration of Fig. 2.1, the output intensity is (assuming $L_L = L_S = L$)

$$P_1 = |\underline{E}_1'\exp[j(\omega_1 t - k_1 L)] + \underline{E}_1'\exp[j(\omega_1 t - k_1(L+\Delta 1))] + \underline{E}_2'\exp[j(\omega_2 t - k_2 L)] + \underline{E}_2'\exp[j(\omega_2 t - k_2(L+\Delta 1))]|^2 \tag{2.14}$$

$$= |\underline{E}_1'\exp[j(\omega_1 t - k_1 L)][1+\exp(-jk_1\Delta 1)] + \underline{E}_2'\exp[j(\omega_2 t - k_2 L)][1+\exp(-jk_2\Delta 1)]|^2. \tag{2.15}$$

Collecting and factoring out the difference phase terms

the laser frequency, laser frequency drift could also cause interferometer output fluctuations. This is of significance in the case of a He-Ne laser which was used for the initial experiments. The major cause of frequency drift of an internal mirror laser, such as a He-Ne laser, is the change in length of the cavity due to thermal expansion and contraction.

The He-Ne laser used in this experiment has two longitudinal modes which are orthogonally polarized. The modes traverse the Doppler broadened gain curve as the cavity thermally expands and contracts (refer to Fig. 2.2). The mode separation is

$$\Delta\nu = c/2\ L(T) \tag{2.10}$$

where c is the speed of light and L(T) is the laser cavity length as a function of temperature. Thus each frequency component of the multi-frequency output of the He-Ne laser drifts over the Doppler profile which is of the order of a GHz.

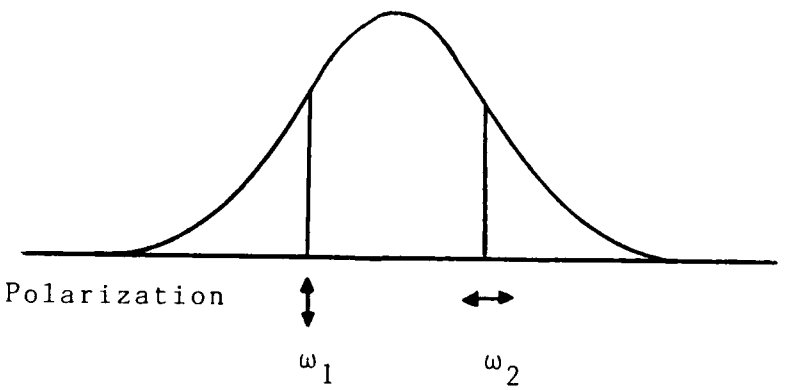

Fig. 2.2 Longitudinal mode distribution of a two mode He-Ne laser. Adjacent modes are orthogonally polarized.

several microns.

Stabilization of the interferometer output is achieved by actively controlling the parameter L_L-L_S. This is accomplished by sensing the fluctuation, $\Delta 1$, through the interferometer output intensity fluctuation, and applying negative feedback via a transducer that varies L_L-L_S accordingly. The net effect is to cancel the fluctuation so that the interferometer output is stable.

Refractive Index Variations

The propagation constant is $k = \omega n/c$, where n is the refractive index of the air in the interferometer path. Equations (2.8) and (2.9) show that refractive index variations will also cause the interferometer output to fluctuate. The refractive index will vary in the presence of air currents since the interferometer is in an open air environment. The effect is observable in the frequency range of approximately sub Hz to a few Hz by introducing an air current disturbance.

2.2 Laser Source Stability

Since the interferometer is stabilized by a laser source, stability of the former is directly determined by the properties of the latter. In this section we review some of the laser related effects.

Because the propagation constant k is proportional to

which gives

$$E_1 = r\underline{E}_S\exp(-jkL_S) + jt\underline{E}_L\exp[-jk(L_L+\Delta 1)] \quad (2.4)$$

$$E_2 = jt\underline{E}_S\exp(-jkL_S) + r\underline{E}_L\exp[-jk(L_L+\Delta 1)]. \quad (2.5)$$

The interferometer output intensities are found from the well known equation for the time average Poynting vector

$$P = \langle ExH^* \rangle/2 = Y_o|E|^2/2 \quad (2.6)$$

where Y_o is the free space admittance. Multiplying the field expression by its conjugate gives the square of the field magnitude. Substituting $r = t = 1/\sqrt{2}$ and Eq. (2.4) into Eq. (2.6) gives

$$P_1 = Y_o[|E_S|^2+|E_L|^2+ 2E_SE_L\cos[k(L_L-L_S+\Delta 1)+\phi_S-\phi_L- \pi/2]]/4 \quad (2.7)$$

Neglecting the constant phase terms, Eq. (2.7) reduces to

$$P_1 = Y_o[|E_S|^2+|E_L|^2+ 2E_SE_L\cos[k(L_L-L_S+\Delta 1)]/4. \quad (2.8)$$

A similar derivation for P_2 yields

$$P_2 = Y_o[|E_S|^2+|E_L|^2- 2E_SE_L\cos[k(L_L-L_S+\Delta 1)]/4. \quad (2.9)$$

Path Length Sensitivity

Notice in equations (2.8) and (2.9) that as $L_L-L_S+\Delta 1$ varies from 0 to $\lambda/4$ the cosine term goes from a maximum to a null for a given wavelength. For a Helium-Neon (He-Ne) laser, $\lambda/4$ = 0.158 micron. Thus for a given (L_L-L_S), a path length jitter of only 0.158 micron in either of the arms will cause the output intensity to fluctuate from a maximum to a minimum. For interferometric work such as optical homodyne detection, one must control $\Delta 1$ to a very high precision, which in a common laboratory environment can be as large as

The equivalent noise circuit of the detector/transimpedance amplifier is shown in Fig. 4.3

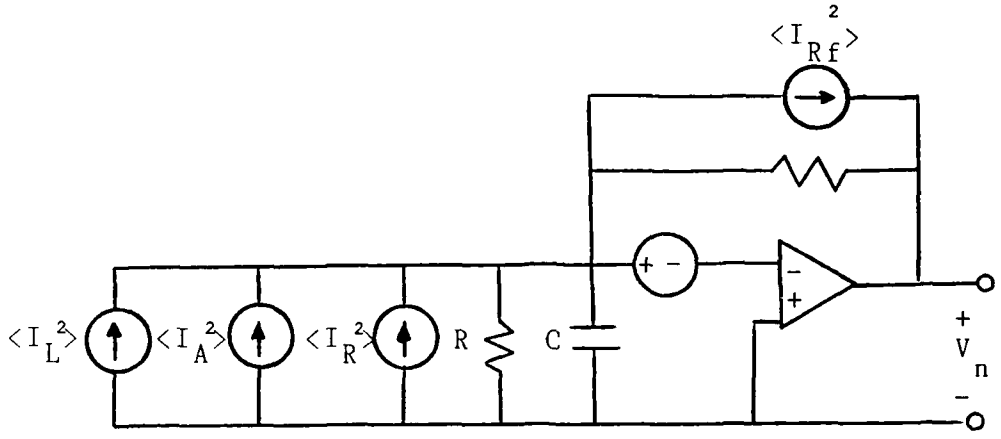

$R = R_{amp} + R_{photodiode}$, V_A = amp input noise voltage

$C = C_{amp} + C_{photodiode}$, I_A = amp input noise curient

$\langle I_L^2 \rangle = 2eI_s$, $\langle I_R^2 \rangle = 4kT/R$, $\langle I_{R_f}^2 \rangle = 4kT/R_f$

Fig. 4.3 Noise Model for the Transimpedance Amplifier.

The output noise spectral density, V_n, is found by superposition of the individual noise sources due to V_A, I_T and I_{R_f},

$$\langle V_n^2 \rangle = I_f^2 R_f^2 , \tag{4.8}$$

where I_f is the total noise current in the feedback path. Superposition gives

$$I_f^2 = 4kT(1/R_f + 1/R) + I_A^2 + 2eI_s + V_A^2[(1/R + 1/R_f)^2 + 4\pi^2 f^2 C^2]. \tag{4.9}$$

The noise spectral density is thus

$$\langle V_n^2 \rangle = [4kT(1/R_f + 1/R) + I_A^2 + 2eI_s + V_A^2[(1/R+1/R_f)^2 + 4\pi^2 f^2 C^2)]R_f^2. \quad (4.10)$$

The total RMS noise is

$$V_N = [\int \langle V_n^2 \rangle \, df]^{\frac{1}{2}} \quad (4.11)$$

so that the output SNR is

$$SNR = I_f R_f / V_N \quad (4.12)$$

$$= \frac{I_s}{f^{\frac{1}{2}}[4kT(1/R_f+1/R)+I_A^2+2eI_s+V_A^2((1/R+1/R_f)+(4/3)\pi^2 C^2 f^2)]^{\frac{1}{2}}}$$

The drawback of this configuration is the potential for instability due to the feedback path around a high impedance, high gain amplifier. High frequency oscillations could occur due to positive feedback arising from parasitic capacitance. This can be avoided by careful layout and by choosing an op amp with an adequate phase margin.

High frequency stabilization can be acheived by shunting the feedback resistor with a capacitor. This forms a lead compensation network which introduces a positive phase shift, thus increasing the phase margin. The capacitor value is selected so that the lead network has a singularity near the crossover frequency.

Let us now examine the amplifier characteristics with the feedback capacitor, C_f present. The circuit schematic and component values are given in Fig. 4.4.

Printed Circuit Board Layout

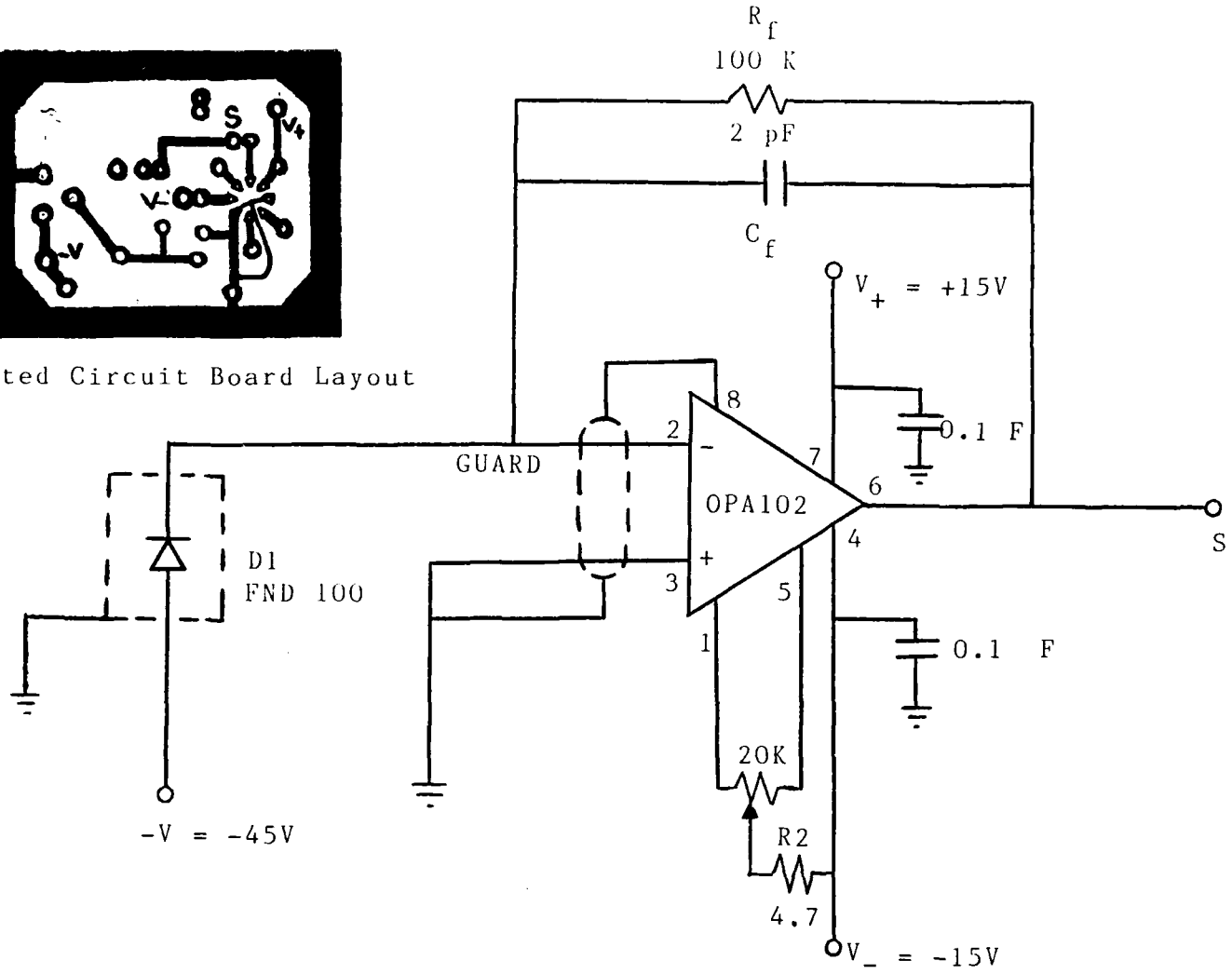

Fig. 4.4 Transimpedance Amplifier

Voltage Noise

The noise voltage gain is

$$\frac{V_o}{V_A} = \frac{A}{1+AB} = \frac{1}{B(1 + 1/AB)}, \qquad (4.13)$$

where A = A(f) is the open loop gain

B = B(f) is the feedback factor

AB = A(f)B(f) is the loop gain.

For AB>> 1 and using node equations, it can be shown that

$$\frac{V_o}{V_A} = \frac{1}{B} = 1 + \frac{R_f(RCs + 1)}{R\ (R_fC_fs + 1)} \qquad (4.14)$$

where $s = j2\pi f$. The transfer function has a zero at

$$f_1 = (R_f + R)/[2\pi R_f R(C_f + C)] \qquad (4.15)$$

and a pole at

$$f_2 = 1/2\pi R_f C_f \qquad (4.16)$$

The component values are

R_f = 100K, R = amp input resistance = 10^{13}

$C = C_{diode} + C_{amp}$ = 10 pF

C_f = 2 pF.

Substitution of these component values gives

f_1 = 133 KHz f_2 = 796 KHz.

The transfer function also shows that in the limits

$$f \to 0 \quad V_o/V_A = 1 + R_f/R \to 1, \qquad (4.17)$$

and $$f \to \infty \quad V_o/V_A = 1 + C/C_f \to 6 \qquad (4.18)$$

To quantify the noise analysis, we need the performance specifications of the operational amplifier. See the Appendix. The Burr Brown OPA102 is a low noise precision

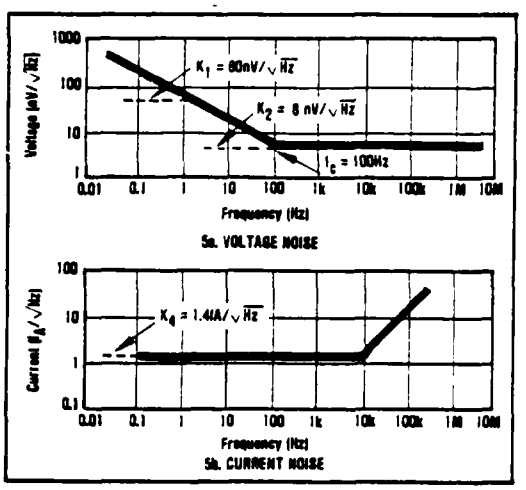

Fig. 4.5 Burr Brown OPA102 low noise op amp voltage noise and current noise spectral density.

JFET input op amp ideally suited for low noise applications. The OPA 102 noise characteristics are shown in Fig. 4.5.

A third corner frequency, f_3, occurs when the closed loop gain curve intersects the open loop gain curve (refer to the specifications). For $f > f_2$, the voltage gain of 6 gives

$$V_o/V_A \text{ (dB)} = 20 \log(6) = 15.6 \text{ dB}.$$

Refering to the spec sheet, an intersection occurs at f = 1MHz. The overall output voltage noise spectral density is shown in Fig. 4.6.

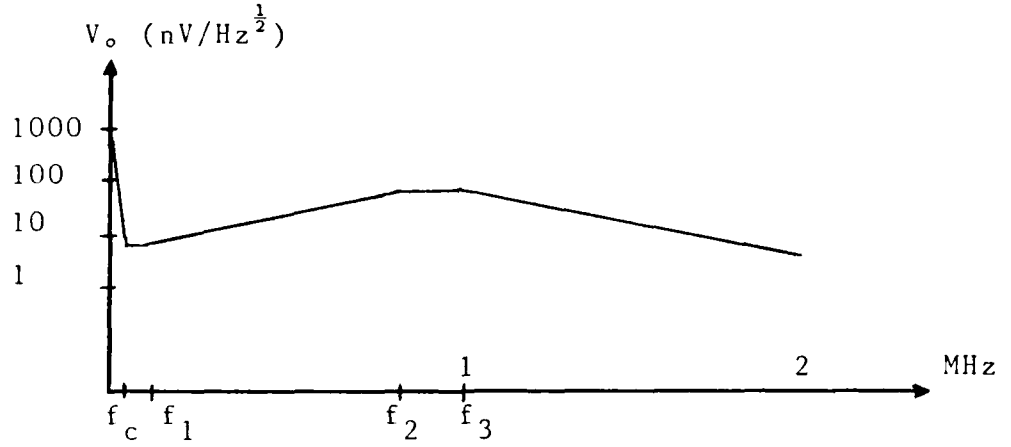

Fig. 4.6 Theoretical output voltage noise spectral density

Current Noise

I_T is the total input noise current due to thermal noise, shot noise and amplifier input current noise. The output voltage noise due to the input current noise is

$$V_o = I_T Z_f(s) = I_T R_f/(R_f C_f s + 1). \quad (4.19)$$

The single pole rolloff frequency for the component values given previously is

$$f_2 = 1/2\pi R_f C_f = 796\text{KHz}. \quad (4.20)$$

The output voltage noise due to input current noise is shown below.

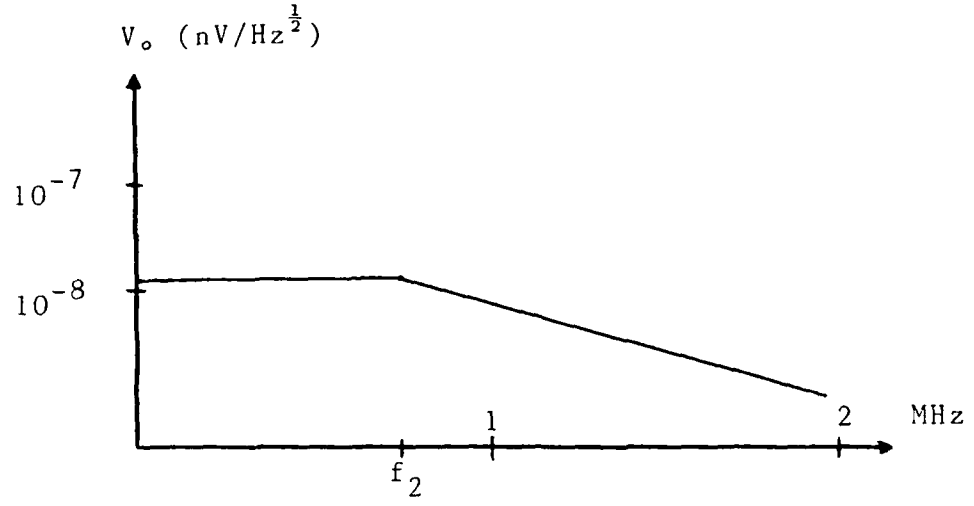

Fig. 4.7 Theoretical output voltage due to noise current.

Theoretical Performance

The total output voltage noise is the sum of the output voltage noise due to the input voltage noise and input current noise,

$$V_n = Z_f \left[(V_A/Z_s)^2 + I_A^2 + \langle I_L^2 \rangle + \langle I_R^2 \rangle + \langle I_{R_f}^2 \rangle \right] \qquad (4.21)$$

where $Z_f = R_f/(1 + 4\pi^2 f^2 C_f^2 R_f^2)$

$Z_s = R/(1 + 4\pi^2 f^2 C^2 R^2)$

V_A = amp input voltage noise = 8 nV/Hz$^{\frac{1}{2}}$

I_A = amp input current noise = 1.4 fA/Hz$^{\frac{1}{2}}$

$\langle I_L^2 \rangle = 2eI_s = 1.08\text{x}10^{-23}$ A/Hz$^{\frac{1}{2}}$

$\langle I_R^2 \rangle = 4kT/R = 1.6\text{x}10^{-29}$ A/Hz$^{\frac{1}{2}}$

and $\langle I_{R_f}^2 \rangle = 4kT/R_f = 1.6\text{x}10^{-25}$ A/Hz$^{\frac{1}{2}}$.

The shot noise term is measured experimentally. For a measured amplifier output voltage of 3.4 V, the incident intensity is $1.87\text{x}10^{-5}$ W for R_f = 100K (see Eqs. (2.24) and (4.4)).

First, consider the case with no light impinging on the detector, i.e., $\langle I_L^2 \rangle = 0$ (thermal noise dominates).

At f = 1 KHz, $Z_f = 10^6$ and $Z_s = 1.6\times10^7$

which gives $V_n = 4.06\times10^{-8} V/Hz^{\frac{1}{2}}$.

At f = 100 KHz, $Z_f = 9.9\times10^4$ and $Z_s = 1.59\times10^5$

which gives $V_n = 4.06\times10^{-8} V/Hz^{\frac{1}{2}}$.

Now consider the case with light impinging on the detector, i.e., $\langle I_L^2 \rangle = 2eI_s = 1.08\times10^{-23}$ (shot noise dominates).

At f = 1KHz, $V_n = 3.31\times10^{-7} V/Hz^{\frac{1}{2}}$

At f = 100 KHz, $V_n = 3.28\times10^{-7} V/Hz^{\frac{1}{2}}$

Since the data will be recorded on a spectrum analyzer, we must convert V to a power spectral density (in dBm) as seen by the input termination of the spectrum analyzer (R_{SA}). The spectrum analyzer resolution, B, corresponds to the bandwidth over which V_n is integrated.

$$P_{SA} = 10 \log \left\{ \frac{V_n^2 B \times 10^3}{R_{SA}} \right\} (dBm) \qquad (4.22)$$

This gives, for the above values with R_{SA} = 50 ohms,

Thermal Noise: f = 1 KHz, P_{SA} = -115dBm for B = 100 Hz

f = 100 KHz, P_{SA} = -100dBm for B = 3 KHz

Shot Noise: f = 1 KHz, P_{SA} = -97 dBm for B = 100 Hz

f= 100 KHz, P_{SA} = -82 dBm for B = 3 KHz

4.3 Experimental Performance

The transimpedance amplifier is built on a printed circuit board using shielding and guarding techniques to minimize noise. In addition, mounting the photodiode on the same board in close proximity to the op amp minimizes stray capacitance, thus improving the frequency response. The printed circuit board is mounted in a metal case for further shielding.

Figure 4.4 shows the circuit schematic. The printed circuit board layout is shown in the inset. Notice the guard ring surrounding the inverting input terminal, pin 2. The purpose of the guard ring is to minimize leakage currents. The op amp case, pin 8, is also connected to the guard potential. This minimizes the voltage across leakage paths, thus minimizing the noise [6].

Power supply decoupling is effected with the 0.1 uF capacitors. Resistors R1 and R2 are output voltage offset null dividers.

D1 is a silicon photodiode, the EG&G FND 100. When reverse biased, it has a junction resistance of 1 Gohm and a junction capacitance of 8.5 pF. The quantum efficiency at 632 nm is experimentally found to be .75. The reverse bias voltage is supplied by a 45 volt battery to avoid power supply noise pickup.

Amplifier thermal noise is measured at the amplifier output with the photodiode aperture blocked. Shot noise is

the amplifier output noise with the laser impinging on the detector. The theoretical shot noise is determined by measuring the photodiode current, I_s. The current is found by measuring the output voltage and dividing by the transimpedance.

$$V = 3.4\ V \Rightarrow I_s = 3.4\times10^{-5} \Rightarrow \langle I_L^2 \rangle = 2eI_s = 1.08\times10^{-23}$$

This is the value used in Eq. (4.20) to find the theoretical shot noise level.

Experimental data is collected with a spectrum analyzer. The laser source is a Metrologic He-Ne laser which operates at 632 nm. Photos of the amplifier noise power spectral densities for thermal noise and shot noise are presented in Figs. 4.8(a)-(h). In all photos, the top center number is the reference level at the top graticule. The lower right number is the frequency span per horizontal division. The right center number is the resolution, B.

Table 1 is a tabulation of the theoretical and experimental data for the power spectrum at 1 KHz and 100 KHz. Table 2 compares the theoretical and experimental corner frequencies as discussed in section 4.2.

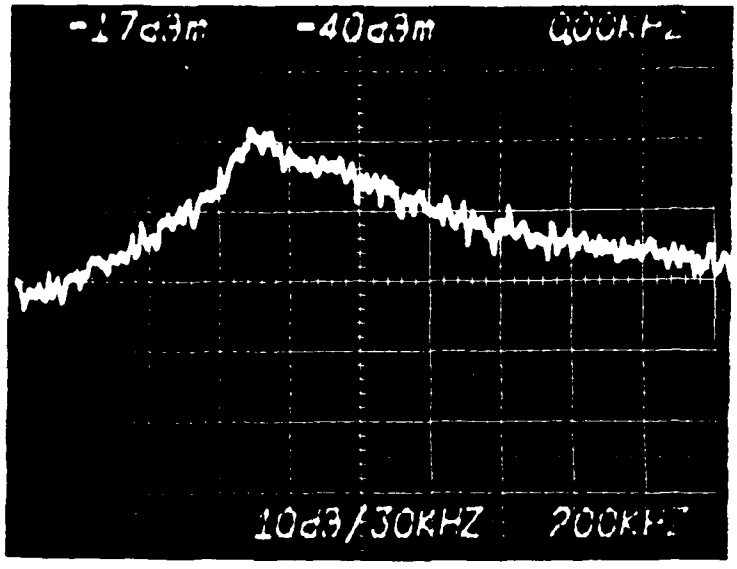

Fig. 4.8(a): Thermal noise spectrum for $0 < f < 2$ MHz.

The spectrum rolls off at $f_3 = 1$ MHz.

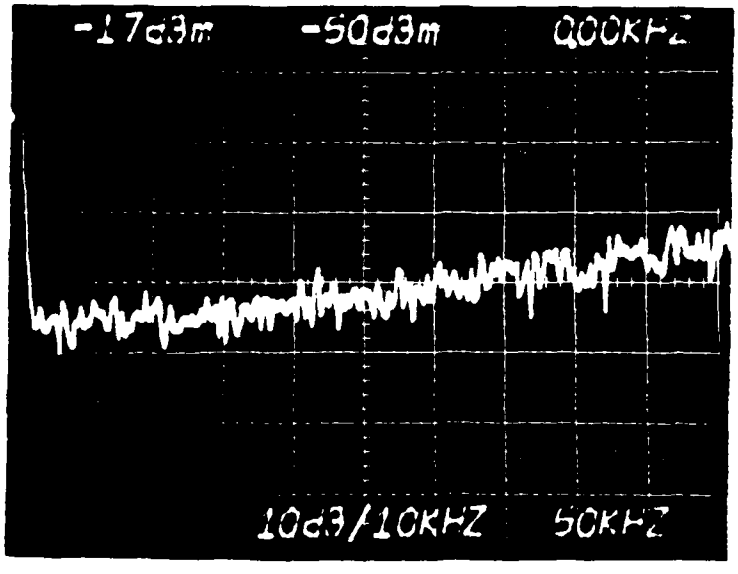

Fig. 4.8(b): Thermal noise spectrum for $0 < f < 500$ KHz.

The spectrum increases at $f_1 = 130$ KHz.

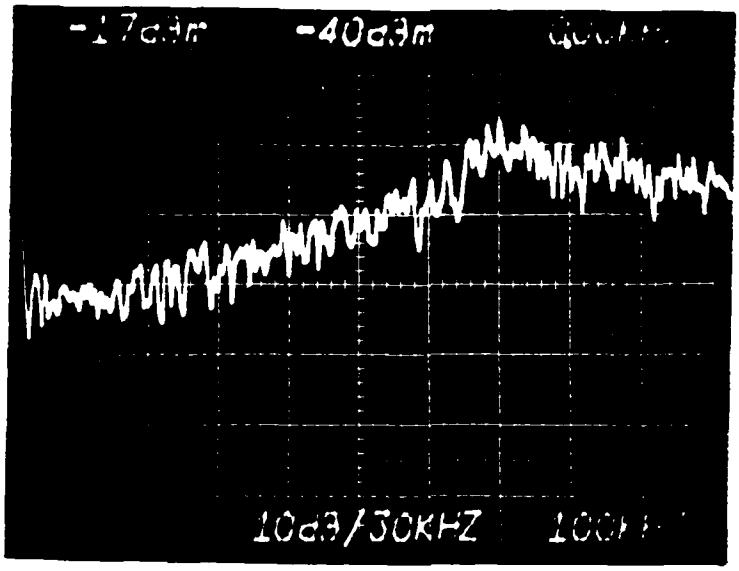

Fig. 4.8(c): Thermal noise spectrum for 0 < f < 1 MHz.
The spectrum levels off at f_2 = 700 KHz.

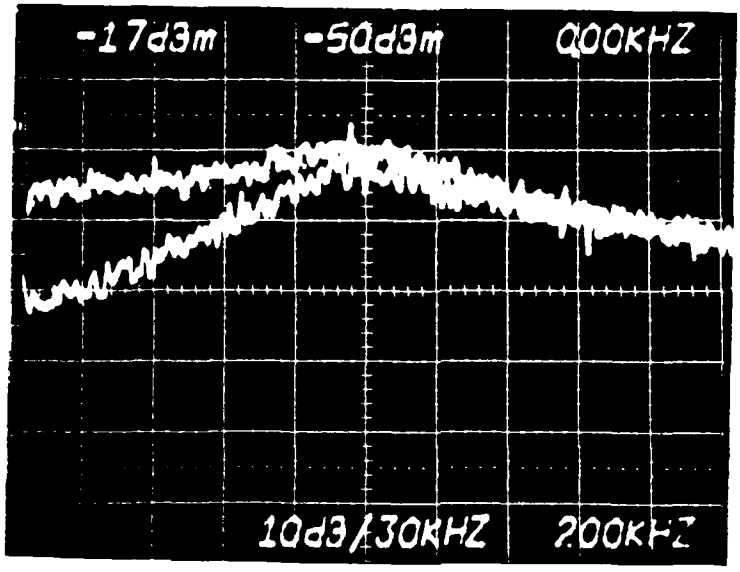

Fig. 4.8(d): Noise spectrum for 0 < f < 2 MHz. Top: shot noise; Bottom: thermal noise.

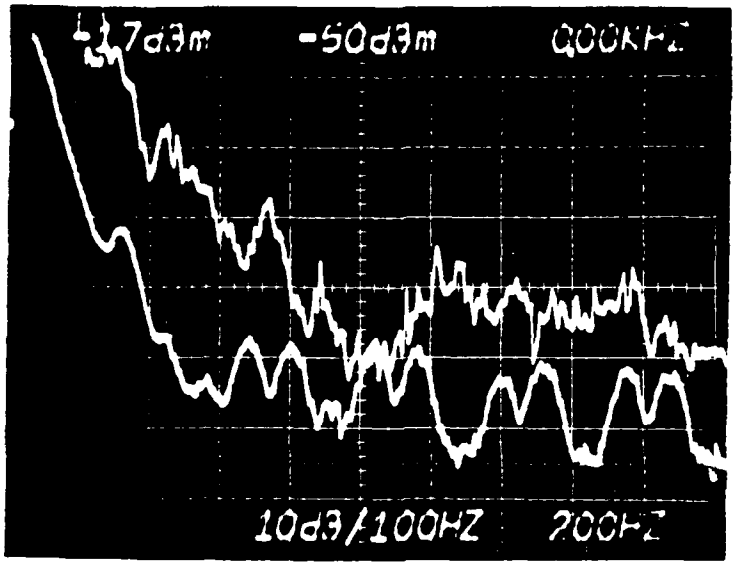

Fig. 4.8(e): Noise spectrum for 0 < f 2 KHz. Top: shot noise; Bottom: thermal noise. Notice the 1/f noise and laser excess noise.

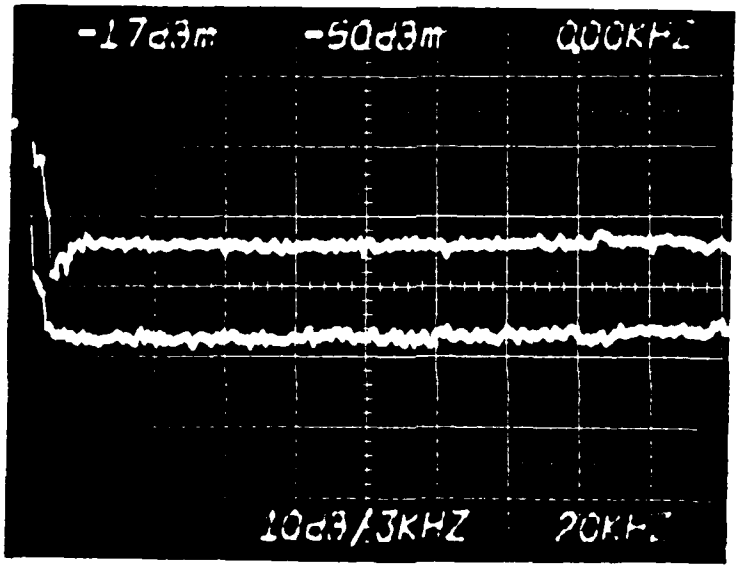

Fig. 4.8(f): Noise spectrum for 0 f 200 KHz. Top: shot noise; Bottom: thermal noise.

TABLE 1: Theoretical vs. Experimental Noise Power				
			Noise Power (dBm)	
Noise	f	B	Theoretical	Experimental
Thermal	1 KHz	100 Hz	-115	-110
	100 KHz	3 KHz	-100	-98
Shot	1 KHz	100 Hz	-97	-100
	100 KHz	3 KHz	-82	-84

TABLE 2: Noise Corner Frequencies		
Corner Frequency	Theoretical	Experimental
f_c	100 Hz	1 KHz
f_1	133 KHz	130 KHz
f_2	796 KHz	700 KHz
f_3	1 MHz	1 MHz

The discrepancy at 1 KHz for the corner frequency f_c can be explained by the fact that the theoretical calculation did not include laser excess noise and amplifier 1/f noise. This is evident in Fig. 4.8(c). The excess noise dominates the amplifier voltage noise corner frequency, f_c, which is specified as 100 Hz (see Fig. 4.5). At higher frequencies, up to 130 KHz, the noise spectrum is flat. The theoretical and experimental values agree well at 100 KHz.

The noise corner frequency f_2 is dependent on the feedback capacitance (see Eq. 4.16). Therefore any stray capacitance would alter the calculated corner frequency. The

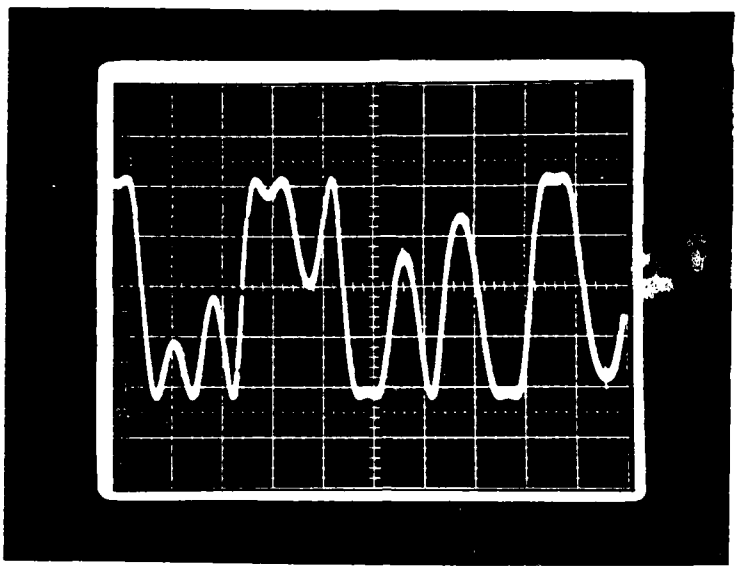

Fig. 5.3(a) Unlocked error signal due to induced noise = 2Vpp (.5V/vertical division and 2 mS/horizontal division).

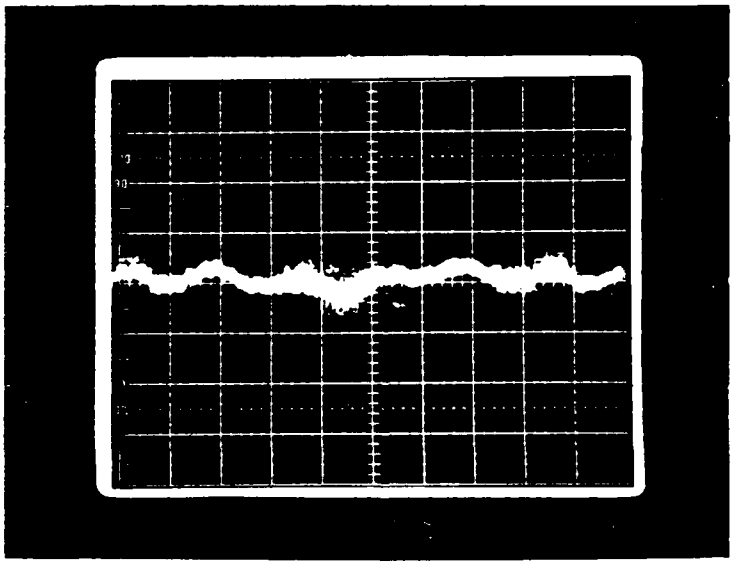

Fig. 5.3(b) Locked error signal = 10 mVpp (20mV/vertical division and 2 mS/horizontal division). High frequency noise is on the Burleigh RC-140 power supply.

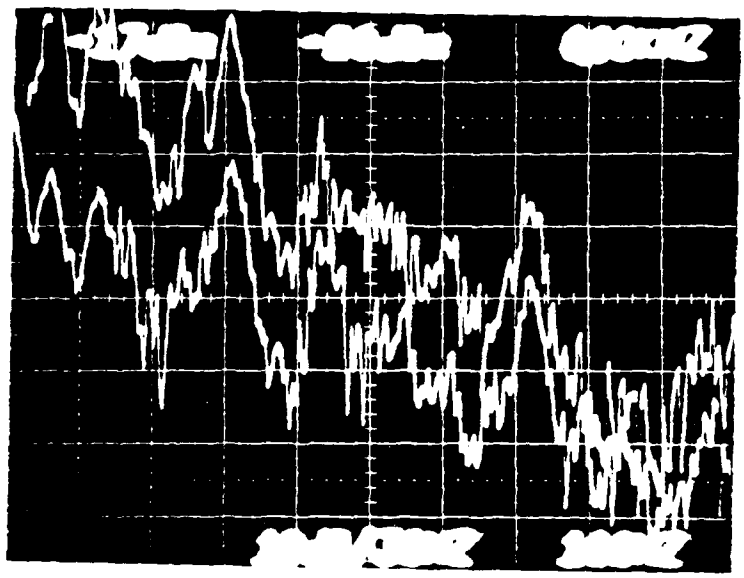

Fig. 5.2(g)

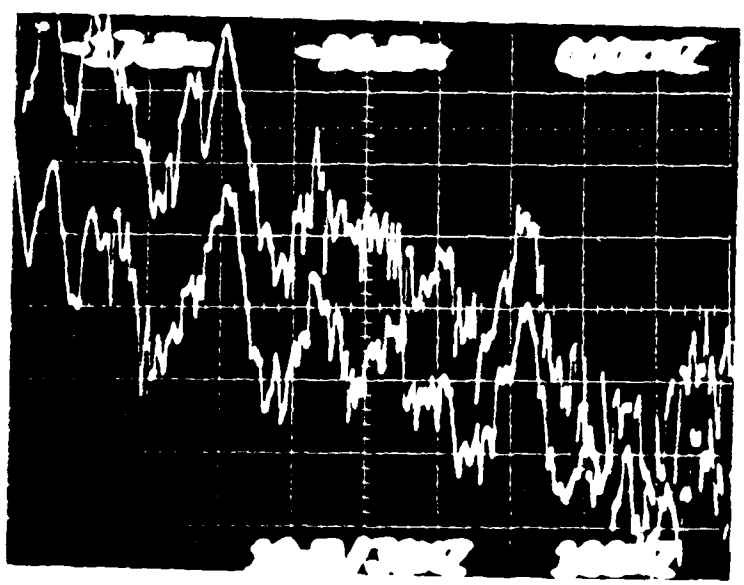

Fig. 5.2(h)

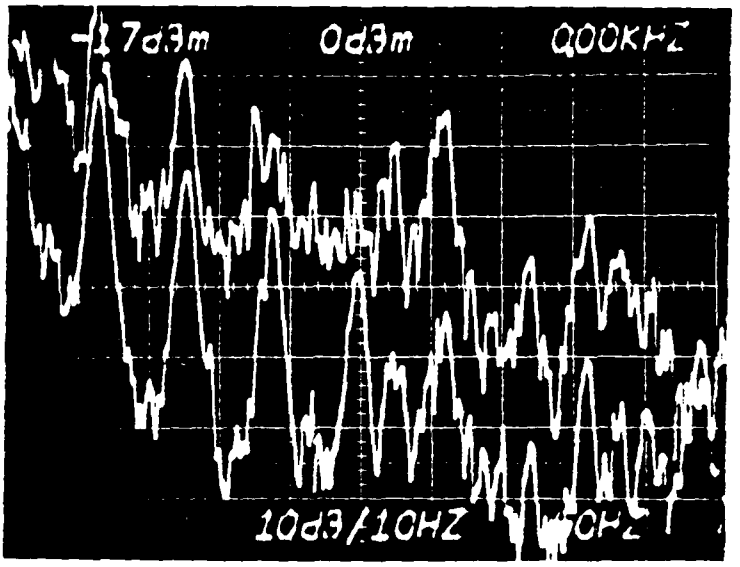

Fig. 5.2(e)

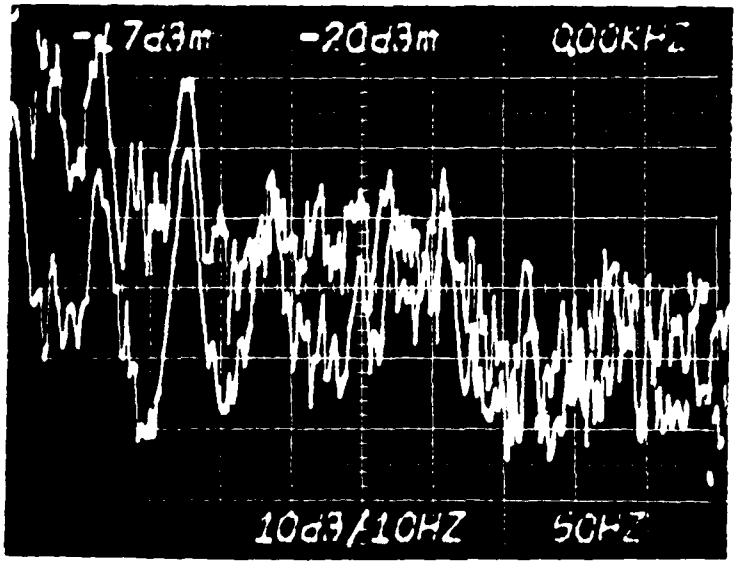

Fig. 5.2(f)

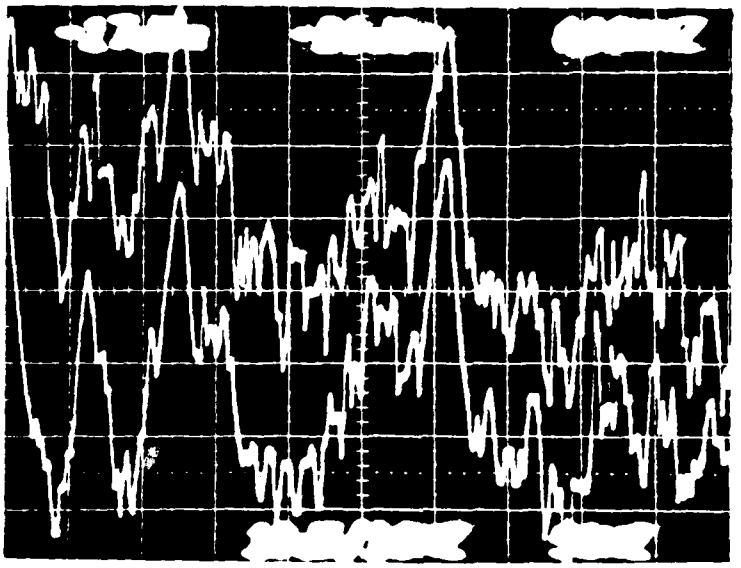

Fig. 5.2(c)

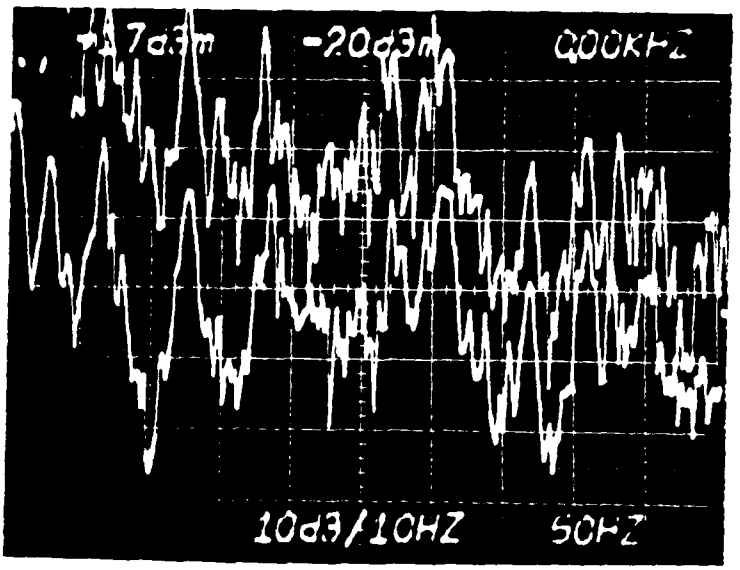

Fig. 5.2(d)

Figs. 5.2(a)-(h): The top traces are the unlocked error signal spectrum. The bottom traces are the locked error signal spectrum. The average of the noise reductions in Figs. 5.2(a)-(h) is used for experimental values.

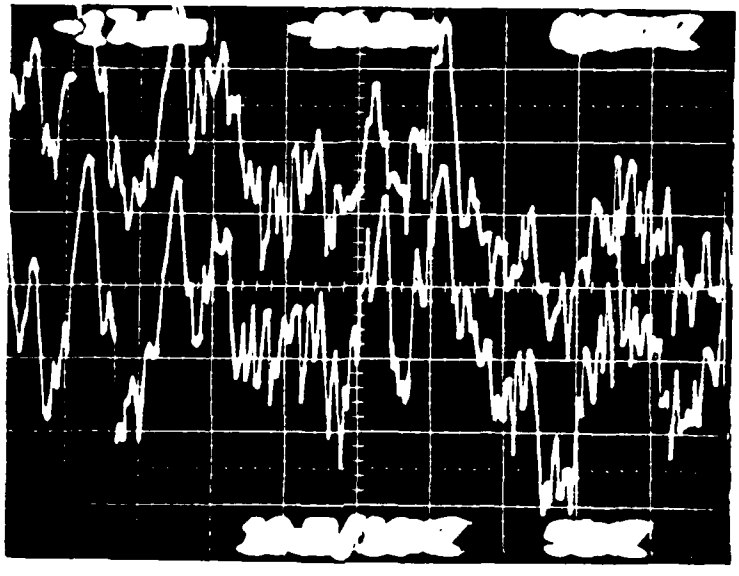

Fig. 5.2(a)

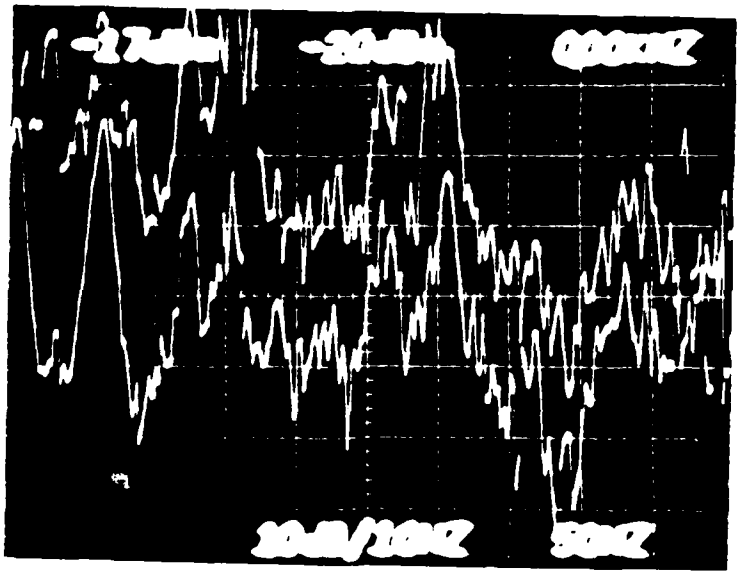

Fig. 5.2(b)

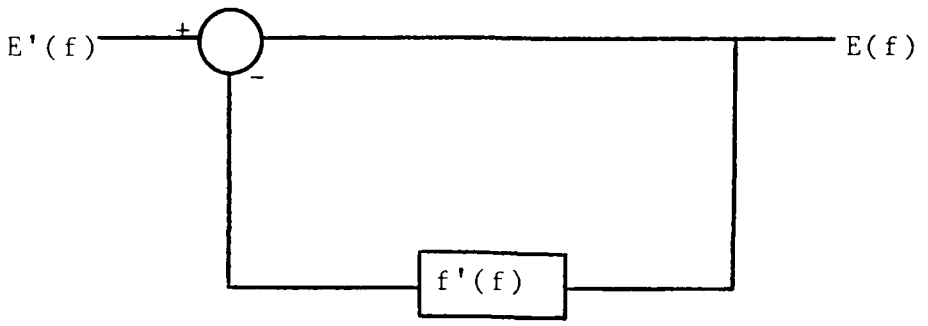

Fig. 5.1: Feedback Error Model

5.4 Experimental Results

The values for G(f) and A(f) are measured experimentally at f = 10 Hz, 100 Hz and 1 KHz. The high voltage amplifier gain A(f), is set so that the system is locked with maximum gain without being unstable.

The interferometer transfer gain, $I = \Delta E/\Delta V$, is experimentally found to be I = .025. Since I must be measured with the system unlocked, it is difficult to measure accurately. Another factor that leads to measurement difficulties is the random nature of the fluctuations. When measuring the unlocked noise levels on the spectrum analyzer, the noise level at high frequencies is dependent on the low frequency noise level. Several runs are measured and the average noise reduction is presented. Spectrum analyzer results are shown for eight trials in Figs. 5.2(a)-(h).

5.3 Feedback Model

The theoretical noise reduction can be determined from the overall loop gain of the feedback loop. A feedback model of the system is shown in Fig. 5.2. A(f) and G(f) represent the gain of the integrator and the high voltage amplifier, respectively. I is the transfer gain of the interferometer measured at the subtractor output with respect to the correction voltage applied to the PZT. The loop gain, f'(f), is the product of the gain of each element

$$f'(f) = A(f)G(f)I \tag{5.13}$$

where $A(f) = 1/RCs$

and $G(f) = 1/[1 + j(f/f_h)]$; f_h is the bandwidth.

The interferometer transfer gain, I, is measured experimentally.

E'(f) is the input reference signal without feedback and E(f) is the error signal with feedback. The feedback factor is found by solving the relationships among the system variables.

$$E(f) = E'(f) - f'(f)E(f)$$

$$E(f) = E'(f)/[1 + f'(f)] \tag{5.14}$$

The feedback factor, in decibels, is

$$N = 10 \log[1/(1-f'(f))] \tag{5.15}$$

Theoretical and experimental noise reduction figures are listed in section 5.4.

A transverse EO phase modulator introduces a phase delay according to [1]

$$\Delta\phi = -\omega n_o^3 r_{63} l V_D/2cd \qquad (5.9)$$

where ω = frequency

n_o = ordinary index of refraction

r_{63} = electrooptic tensor coefficient

c = free space velocity of light

V_D = error drive voltage

d = crystal width

l = crystal length

For an incident field, $\hat{y}\ E_o\cos[(\omega t - z/c])$ polarized along a crystal principal axis, the EO output field is

$$\overline{E}_{out} = \hat{y}\ E_o\cos[\omega(t - (z-l)/c) - \psi]$$

where $$\psi = (\omega l/c)[n_o + (n_o r_{63} V_D)/2d] \qquad (5.10)$$

Neglecting the constant phase terms

$$E_{out} = \hat{y}\ E_o\cos(\omega t - KV_D) \qquad (5.11)$$

where $K = n_o^3 r_{63} l/2cd$.

The detector error signal voltage in this case is

$$E = Y_o(e\eta RP/h\nu)E_S E_L \cos(k\Delta l + KV_D) \qquad (5.12)$$

Note that the correction term is wavelength dependent. A proposed stabilization scheme was to use a He-Ne laser for stabilization and a dye laser for the signal carrier. However, because of the wavelength dependence of the correction term, the dye laser signal would not see the same correction as the He-Ne laser. For this reason, the PZT scheme was chosen for stabilization.

cosine response curve. This gives an error signal equal to zero when the system is locked.

5.2 Feedback Transducer

Piezo Electric Transducer

The PZT drives a mirror in one arm of the interferometer. The PZT expands linearly with an applied voltage according to

$$\Delta l = d_{31} L V_D / W \qquad (5.8)$$

where d_{31} = material constant = .171 nm/V

L = PZT length = 900 mil

V_D = applied voltage

W = PZT thickness = 121 mil

To move the mirror a quarter wavelength (632.8/4 nm for He-Ne) requires V =125 V.

Electro-optic Modulator

An electro optic modulator configured as a phase modulator can be used instead of the PZT to compensate for path length variations. The EO modulator is placed in the signal arm and introduces a phase delay proportional to the error signal.

the output offset voltage of the op amp.

Integrator

The function of the integrator is to integrate the error signal so that a correction voltage is applied to the PZT until the error signal is zero. This can be readily seen by considering the following case. Suppose the error signal is a constant voltage. The integrator output is a ramp so that a correction voltage is applied to the transducer until the error signal is zero.

The integrator output for an input error signal E is

$$V = -1/RC \int E \, dt \tag{5.6}$$

The frequency response of the integrator is found from the transfer function

$$A(f) = 1/2\pi fRC. \tag{5.7}$$

The closed loop gain at DC is limited by the open loop gain of the op amp and rolls off at 20 dB per decade.

High Voltage Amplifier

A high voltage amplifier is necessary to drive the PZT or electrooptic modulator. The amplifier used in the experiments is a Burleigh RC-140 high voltage amplifier. The overall loop gain is controlled at this stage by means of a variable gain. A variable DC bias is used to adjust the operating point. The operating point is chosen so that the feedback phase is negative and at the zero crossing of the

Subtractor

The advantage of a dual detection scheme is discussed in Chapter 2. First, it eliminates the need for a biasing circuit which subtracts the DC voltage due to the first two terms of EQ. (5.1) and (5.2). Second, it makes the feedback error signal insensitive to laser intensity fluctuations.

The output of the subtractor is the desired error signal. Since the fluctuations are at acoustic frequencies the subtractor bandwidth does not need to be very large. Subtraction is implemented with an op amp differential amplifier. Refering to Fig. 5.1, the general transfer function is

$$E = [(R1+R3)/R1][R4/(R2+R4)]V1 - (R3/R1)V2, \qquad (5.3)$$

where V1 and V2 are the output voltages of the transimpedance amplifiers. The resistors R1 - R4 are chosen equal so that the subtractor is of unity gain. This gives

$$E = V1 - V2$$

$$= -4(Y_o e\eta R_f/4h\nu)E_S E_L \cos[k(L_L - L_S + \Delta l) \qquad (5.4)$$

This is the desired error signal. Notice that the error signal is zero when the system is stabilized, i.e., when

$$L_L - L_S + \Delta l = m\lambda/4, \quad \text{where } m = \text{integer}. \qquad (5.5)$$

A DC offset is present at the subtractor output when the interferometer output intensities are unequal. This occurs when the output beam splitter is not a 50/50 beam splitter. An offset potentiometer is used to null the subtractor output when this is the case. The offset potentiometer a'so nulls

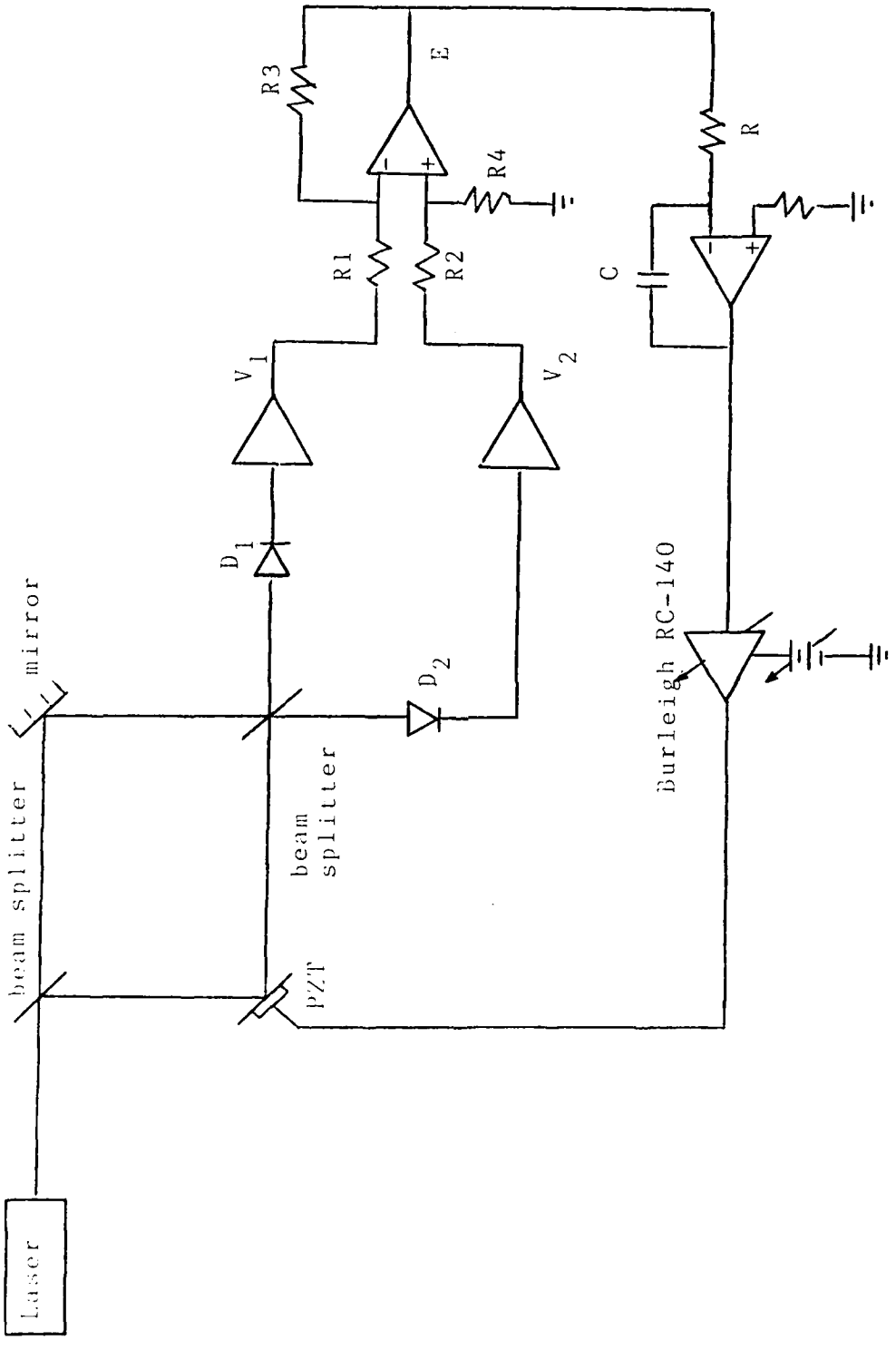

Fig.5.1: Feedback Stabilization Loop

CHAPTER 5

OPTICAL FEEDBACK STABILIZATION

5.1 Feedback Electronics

Stabilization of the interferometer is achieved by a feedback loop that correlates the path lengths in the two arms of the interferometer. This is accomplished by deriving an error signal from the interferometer output fluctuations. This error signal is amplified and fed to a stabilization transducer (either an EOM or a PZT) which changes either the phase or path length of one of the arms. The feedback loop shown in Fig. 5.1 is comprised of the following elements:

Detector/Amplifier

The transimpedance amplifier is discussed in detail in Chapter 4. The detector converts the incident optical power to a current proportional to the intensity. The current is then converted to an output voltage by the transimpedance amplifier. The output voltages are

$$V1 = -I_1 R_f$$
$$= -(Y_o e\eta R_f/4h\nu)[|E_S|^2+|E_L|^2+ 2E_S E_L \cos[k(L_L-L_S+\Delta 1)] \quad (5.1)$$
$$V2 = -I_2 R_f$$
$$= -(Y_o e\eta R_f/4h\nu)[|E_S|^2+|E_L|^2- 2E_S E_L \cos[k(L_L-L_S+\Delta 1)] \quad (5.2)$$

As discussed in the following section, an error signal is derived from the output fluctuations on V1 and V2. The error signal is proportional to the cosine of the path length variations as shown in the equations above.

corner frequencies, f_1 and f_3 correlate very well.

Based on the experimental data, the transimpedance amplifier performed as designed. In Chapter 5, the transimpedance amplifiers will be implemented in the feedback stabilization loop.

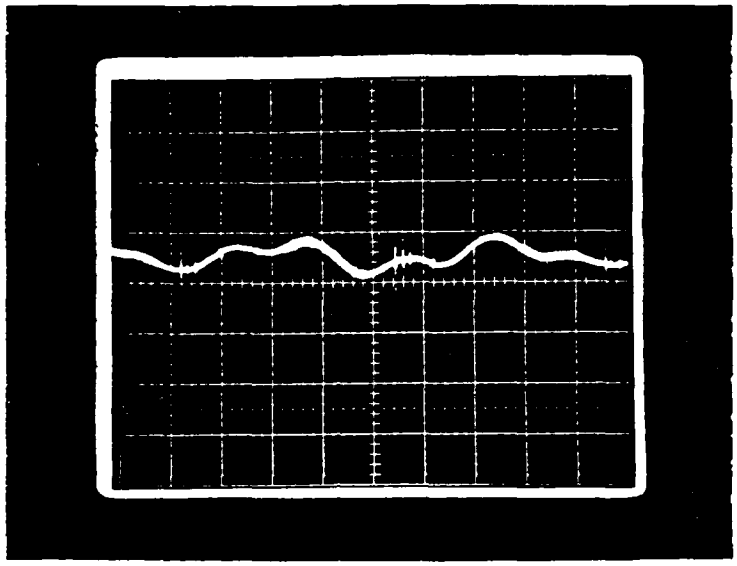

Fig. 5.3(c): Unlocked error signal = .2 Vpp due to noise in the lab. (0.2V/vertical division and 2 mS/horizontal division)

The measured loop gain and corresponding noise reduction at f = 10 Hz - 100 Hz and f = 900 Hz - 1 KHz are presented in Table 3. The theoretical values are also listed for comparison.

TABLE 3

EXPERIMENTAL VS. THEORETICAL NOISE REDUCTION

Freq.	G(f)	A(f)	f'(f)	Noise Reduction	
				Experimental	Theoretical
10-100 Hz	55	80	109	-21dB	-20dB
900-1 KHz	3	80	6	-10dB	-8.5dB

RMS Noise Reduction

The RMS noise reduction is measured for two cases. First, noise is induced so that the peak to peak unlocked error signal spanned the full error range. Fig. 5.3(a) shows this range to be 2.0 V. The system is then locked to a level of 10 mV as shown in Fig. 5.3(b). The noise reduction is

$$N = 10 \log(.01/2) = -23dB .$$

The second case is for the ambient noise level in the lab (Fig. 5.3(c)). The peak to peak unlocked noise is 0.2 V. The locked level is again 10 mV. The reduction in this case is

$$N = 10 \log(.01/.2) = -13dB .$$

In summary, the stabilization loop reduces the RMS noise level by 13 to 23 dB. As a function of frequency, the noise reduction is 21 dB at 10 Hz - 100 Hz and 10 dB at 900 Hz - 1 KHz. In Chapter 6, the stabilization scheme is applied to a homodyne modulation experiment.

CHAPTER 6

HOMODYNE DETECTION USING A STABILIZED INTERFEROMETER

The experiment to be stabilized is a dual detection homodyne system as discussed in chapter 1. It is shown in Fig. 6.1. The signal arm is field modulated with an electro-optic modulator driven by a sinusoidal voltage source. Without stabilization, the modulation signal has a randomly fluctuating amplitude. As described in Chapter 1, observation of the interferometer output on a spectrum analyzer reveals a fluctuating peak at $\omega_m/2\pi$ and a stable peak at ω_m/π. The analysis to follow will explain the reason for this behavior. It will be demonstrated that the optical feedback stabilization scheme, as discussed in the previous chapter, reduces these fluctuations to a level which allows its detection at the quantum limit.

6.1 Experimental Details

When configured as a field modulator, the EOM driven by a $\sin\omega_m t$ source modulates the incident signal field, $E_S = E_s\exp[-j(kv+\omega_s t)]$, so that

$$E_S' = 2\,E_S\sin\omega_m t \qquad (6.1)$$

The factor of 2 is carried through to cancel a factor which appears when substituting Eq. (6.1) into Eq. (2.6) and to cancel the $1/\sqrt{2}$ factors for the transmission and reflection coefficients of a 50/50 beam splitter.

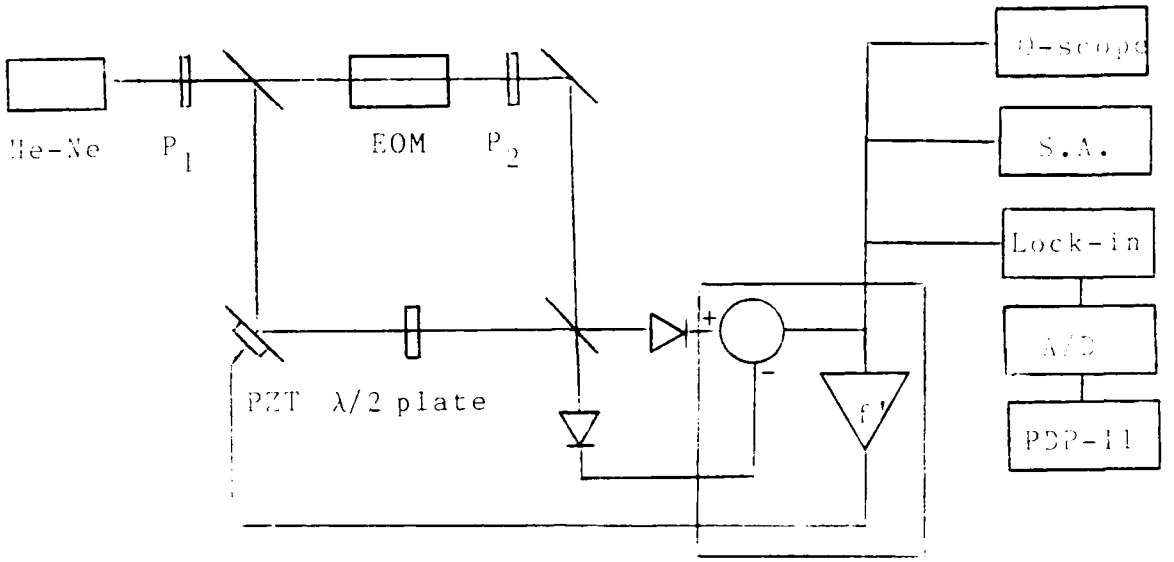

Fig. 6.1 Homodyne Modulation Experiment

To function as a field modulator, the EO modulator must be oriented so that the incident polarization is 45 degrees relative to the crystal's principal axes. This is accomplished with the input polarizer as shown in Fig. 6.2. The output polarizer is oriented so that it is orthogonal to the input polarizer.

The applied field, E_z, changes the index ellipsoid of the crystal so that the indices n'_x and n'_y along the new principal axes are given by [2]

$$n'_x = n_o - n_o^3 r_{63} E_z/2 \qquad (6.2)$$

$$n'_y = n_o - n_o^3 r_{63} E_z/2 \qquad (6.3)$$

and the extraordinary index of refraction remains unchanged,

$$n_z = n_e \ . \qquad (6.4)$$

For an incident field

$$E_{in} = E_i \cos[\omega t - y'(2\pi/\lambda)](\hat{x}' + \hat{z})/\sqrt{2}, \qquad (6.5)$$

the field components along $\hat{x}'$ and $\hat{z}$ experience phase retardations so that the total field transmitted by the orthogonal output polarizer is

$$\bar{E}_{out} = E_o[\exp(-j\omega(t-(y-1)/c)n'_x)\ \hat{x}' - \exp(-j\omega(t-(y-1)/c)n_z)\ \hat{z}]/\sqrt{2} \quad (6.6)$$

Defining ϕ as

$$\phi = (\omega l/2c)(n'_x - n_z) = (\omega l/2c)[n_o - n_e - r_{63}n_o^3 V(t)/2h] \quad (6.7)$$

and

$$\psi = (\omega l/2c)(n'_x + n_z) = (\omega l/2c)(n_o + n_e - r_{63}n_o^3 V(t)/2h), \quad (6.8)$$

the field transmitted at the output polarizer is

$$\bar{E}_{out} = E_o \sin(\phi/2)\sin[\omega(t-(y-1)/c) - \psi\ ](\hat{x}'-\hat{z})/\sqrt{2}. \quad (6.9)$$

Thus the signal field is modulated at frequency ω_m for $V(t) = V\sin\omega_m t$. Notice also that the signal field is polarized orthogonal to the LO field. A half wave plate is placed in the LO arm to rotate the LO field 90 degrees, allowing the signal and LO fields to interfere.

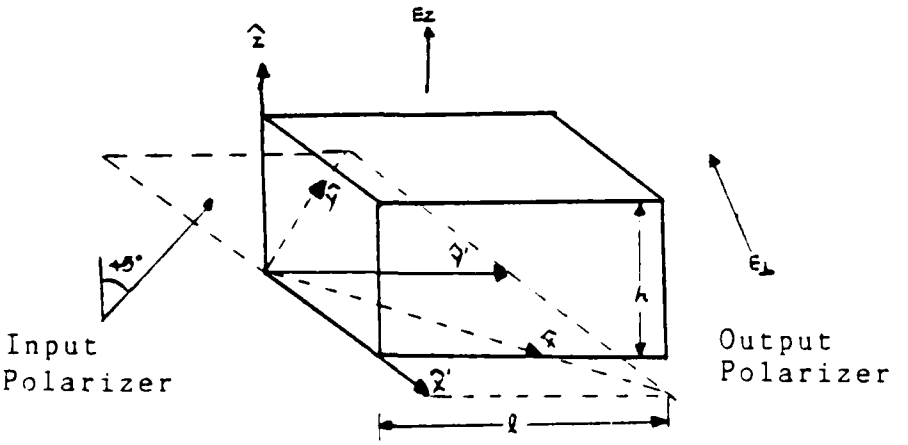

Fig. 6.2 Transverse EOM configured as an amplitude modulator.

Following an analysis similar to that of Sec. 2.1, the output intensity of the interferometer at detector D1 is

$$P_1 = Y_o[\,|E_S|^2 \sin^2\omega_m t + |E_L|^2 + 2E_S E_L \cos[k(L_L - L_S + \Delta 1)]\sin\omega_m t] \quad (6.10)$$

Note that the first term contributes a DC term and a harmonic at $2\omega_m$, while the cross term is at ω_m.

During the experiment, attempts to completely field modulate the signal arm resulted in a weak signal intensity, making it difficult to stabilize the interferometer. This problem was circumvented by modulating at less than 100%, i.e. an unmodulated component is summed with the modulated component, so that the signal field is now

$$E_S' = E_S(1 + \cos\omega_m t). \quad (6.11)$$

The interferometer output intensities for this case are

$$P_1 = Y_o[(1-\varepsilon)|E_S|^2(2 + 2\cos\omega_m t + \cos^2\omega_m t) + \varepsilon|E_L|^2 + \sqrt{\varepsilon(1-\varepsilon)}\,E_S E_L(1 + \cos\omega_m t)\cos k(L_L - L_S + \Delta 1)] \quad (6.12)$$

$$P_2 = Y_o[\varepsilon|E_S|^2(2 + 2\cos\omega_m t + \cos^2\omega_m t) + (1-\varepsilon)|E_L|^2 - \sqrt{\varepsilon(1-\varepsilon)}\,E_S E_L(1 + \cos\omega_m t)\cos k(L_L - L_S + \Delta 1)] \quad (6.13)$$

Notice that now there are two terms which contribute to the signal at frequency ω_m, one due to $2E_S\cos\omega_m t$ which remains stable and a fluctuating component due to $E_S E_L \cos(\omega_m t)\cos[k(L_L - L_S + \Delta 1)]$. The dual detection scheme with 50% beam splitters and matched detectors cancels the E_S and E_L terms of Eqs. (6.12 and 6.13). In the experiment, however, it was difficult to achieve a 50-50 split of the signal field while maintaining a 50-50 split of the [illegible]. It was also observed that the frequency response of the [illegible]

detectors differed by 2 dB at a frequency of 500 KHz . For these reasons, the signal at frequency has a nonzero mean after subtraction since the E_S term is not completely cancelled. The fluctuations due to the last terms of Eqs. (6.12 and 6.13) are superimposed on this mean value. When the system is stabilized, the peak at ω_m remains stable.

6.2 Theoretical Noise Level

If the stabilization eliminates the fluctuations to the level of the quantum limit of photodetection, the minimum system noise level is the shot noise due to the laser. The theoretical shot noise level is found as follows. The mean square current spectral density for each detector is

$$\overline{I_L^2} = 2eI_S B = 2e^2 P\eta / h\nu . \qquad (6.14)$$

The transimpedance, R_f, gives an output voltage spectral density

$$\overline{V_o^2} = \overline{I_L^2} R_f^2$$
$$= 2e^2 P\eta B R_f^2 / h\nu . \qquad (6.15)$$

Making the identification,

$$V = P e\eta R_f / h\nu , \qquad (6.16)$$

Eq. (6.15) reduces to

$$\overline{V_s^2} = 2eVR_f B . \qquad (6.17)$$

6.3 Experimental Results

The measurement apparatus includes an oscilloscope, a spectrum analyzer, a lock-in amplifier and a DEC MINC (Modular INstrument Computer) which has an analog to digital converter (ADC) to process the lock-in amplifier output. The lock-in amplifier produces an output proportional to the noise power density of the subtractor output. The noise equivalent bandwidth of the lock-in amplifier is equal to $1/4\tau$, where τ is the user selectable time constant of the output filter. Another variable parameter is the input sensitivity of the lock-in amplifier and a 10x scale. These settings will determine the measured noise voltage as shown later. The computer runs a program which computes the mean and standard deviation (SD) of the lock-in amplifier output at a predetermined sample rate for 1000 samples. The sample rate is chosen to be much less than the modulation frequency so that the sampled voltage is over many cycles of the modulation frequency.

The quantum shot noise level is established by substituting an incoherent white light source for the laser. The noise produced by the detectors in this manner is quantum limited [7]. The transimpedance amplifier output voltages are set equal to V1 = 1.1 V and V2 = 1.0 V when illuminated by the incoherent source. These values are chosen so that they equal the voltages for the case when the system is locked with the He-Ne laser. Thus, if the He-Ne laser shot

noise equals that of the incoherent light, the stabilization is achieving the quantum limit of photodetection. Substituting V = V1+V2 = 2.1 V into Eq. (6.17), the theoretical RMS shot noise level for R = 100K and B = 250 Hz is

$$V = [eVR\ B] = 2.9\mu V.$$

The experimental measurements are at f = 500 KHz. This frequency is chosen since the transimpedance amplifier and subtractor thermal noise is 5 dB below the shot noise level for the above values of V1 and V2. Measurements are also taken at 100 KHz and 250 KHz, however, noise in excess of the shot noise level is present on the interferometer output and on the transimpedance amplifiers in the frequency range from 80KHz to 300 KHz as shown in Fig. 6.3(a). Experimental data for the incoherent source and the He-Ne laser is collected with the lock-in amplifier and processed with the MINC. Results are given in Table 4.

TABLE 4
Experimental Shot Noise Level

White Light		He-Ne Laser	
Mean	SD	Mean	SD
-19.7	159.40	-307.75	159.97
-19.2	154.30	-309.95	155.23
-23.4	159.33	-303.75	158.09
-15.7	155.31	-306.60	153.66
-19.9	162.51	-301.89	151.17
-10.7	156.58	-302.74	157.80
-16.3	156.19	-309.43	152.19
-29.0	152.80	-313.95	157.94
-13.3	156.90	-304.37	158.40
-12.0	156.79	-312.66	155.56

The data in Table 4 is the MINC output for V1 = 1.1 V and V2 = 1.0 V. The He-Ne laser measurements are for the stabilized interferometer. The lock-in amplifier sensitivity is 100 μV with a full scale range of 400. The data is for the 10x scale and 1 ms time constant. The MINC sample rate is 1000 samples/sec. To reduce the data to the noise level, multiply the average SD by the scale factors as shown below. For the white light, the average SD is 157.01. The noise level is

$$157.01 \times 100\ \mu V/(400 \times 10) = 3.92\ \mu V.$$

The He-Ne laser stabilized interferometer has an average SD equal to 156.0 V. The noise level for this case is

$$156.00 \times 100\ \mu V/(400 \times 10) = 3.90\ \mu V.$$

These numbers, however, include the noise due to the transimpedance amplifiers, subtractor and measurement apparatus. The true measured shot noise level is found by subtracting the noise present when the detectors are blocked. The average SD with the detectors blocked is 82.3, so the adjusted shot noise levels are

$$[157.01^2 - 82.3^2]^{\frac{1}{2}} \times 100\ \mu V/4000 = 3.34\ \mu V$$

and

$$[156.00^2 - 82.3^2]^{\frac{1}{2}} \times 100\ \mu V/4000 = 3.31\ \mu V.$$

for the white light and He-Ne stabilized interferometer, respectively. Recall that the predicted value is 2.9 μV.

Table 5 lists data for an unstabilized and stabilized interferometer. The modulation signal is at 500 KHz and the lock-in amplifier sensitivity is 100 μV on the 10x scale.

The full scale deflection is 400. The time constant is 0.01 s and the MINC sample rate is 100 samples/sec.

TABLE 5
Unstabilized vs. Stabilized Interferometer Fluctuations

Unstabilized		Stabilized	
Mean	SD	Mean	SD
-299.98	174.46	-378.62	46.59
-318.22	136.73	-380.02	46.22
-226.33	142.35	-377.22	45.61
-243.21	111.28	-381.23	46.48
-206.95	174.63	-381.61	46.77
-227.85	244.03	-379.62	47.11
-267.58	156.77	-381.49	45.32
-306.16	106.28	-378.56	48.12
-291.42	103.01	-378.59	47.06
-263.30	128.16	-382.62	45.68
-148.25	231.03	-379.09	48.81
-304.45	110.00	-384.55	45.05
-301.31	101.64	-383.12	47.02
-194.43	180.99	-382.84	48.04
-346.98	100.78	-381.23	47.90
- 64.83	223.67	-380.93	48.41
-155.25	249.74	-380.81	45.65

The average SD with the system locked is 46.4. Again, to compute the true shot noise level, the noise due to the transimpedance amplifiers, subtractor, lock-in amplifier and MINC must be subtracted from the data. For this sensitivity and time constant, the average SD with both detectors blocked is 25.6. Thus the measured shot noise is

$$V_s = [(46.4)^2 - (25.6)^2]^{\frac{1}{2}} \times 100\ \mu V/4000 = 0.96\ \mu V.$$

To confirm that this level is shot noise limited, the detectors are illuminated with a white light source with the same intensities on each detector, V1 = 1.1 V and V2 = 1.0 V. The average SD for this case is 46.6 so that the measured

shot noise is

$$V_o = [(46.6)^2 - (25.6)^{\frac{1}{2}}] \times 100\ \mu V/4000 = 0.97\ \mu V.$$

The theoretical shot noise level for V1 = 1.1 V, V2 = 1.0 V, R_f = 100 K and B = 25 Hz is

$$V_o = [eVR_fB]^{\frac{1}{2}} = 0.92\ \mu V.$$

Notice that the mean for the stabilized case in Table 5 remains relatively constant while the unstabilized mean fluctuates randomly. Fig. 6.3(a) shows the spectrum analyzer display for the He-Ne stabilized interferometer with a 500 KHz modulation signal. Fig. 6.3(b) is the spectrum analyzer display for the white light with the same intensities as in Fig. 6.3(a). Figs. 6.3(c) and 6.3(d) show the spectrum analyzer displays for two levels of modulation at 500 KHz. Fig. 6.3(e) is for a modulation signal at 250 KHz with the arrow showing the fluctuation range when the interferometer is not stabilized. The stabilized output is shown in Fig. 6.3(f).

In summary, the noise on the output of the stabilized interferometer is quantum limited as verified by the white light tests. The difference between the measured and predicted shot noise levels could be due to the tolerance on R_f in the transimpedance amplifiers and deviations from the specified noise equivalent bandwidth of the lock-in amplifier.

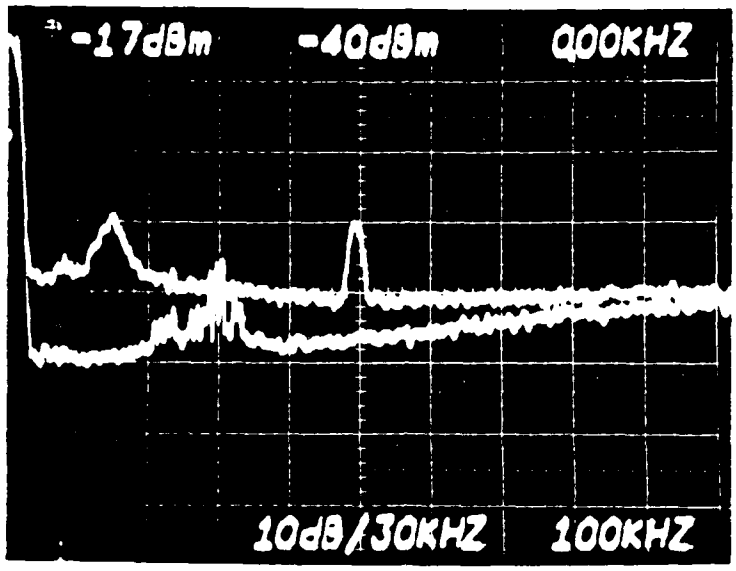

Fig. 6.3(a)
Top: Subtractor output of locked interferometer with a modulation signal at f_m = 500 KHz. The detector voltages are D1 = 1.1 V and D2 = 1.0 V. Bottom: Subtractor output with both detectors blocked.
The peak at 150 KHz is present when beating the signal and LO. The noise at 300 KHz is due to the transimpedance amplifier power supply.

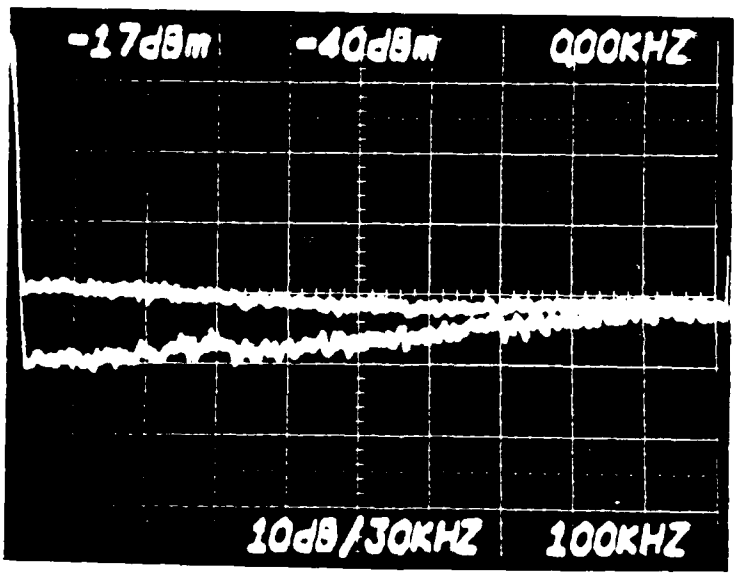

Fig. 6.3(b)
White light test with D1 = 1.1 V and D2 = 1.0 V. Top: Subtractor output. Bottom: Both detecters blocked.

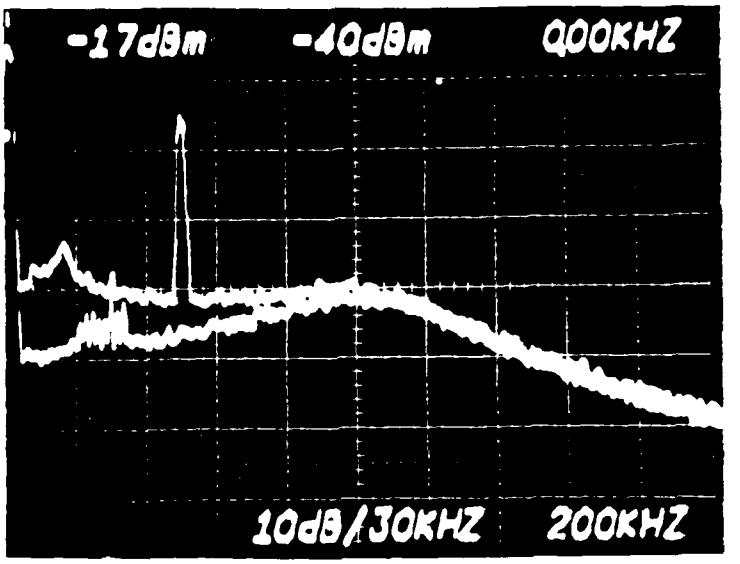

Fig. 6.3(c)

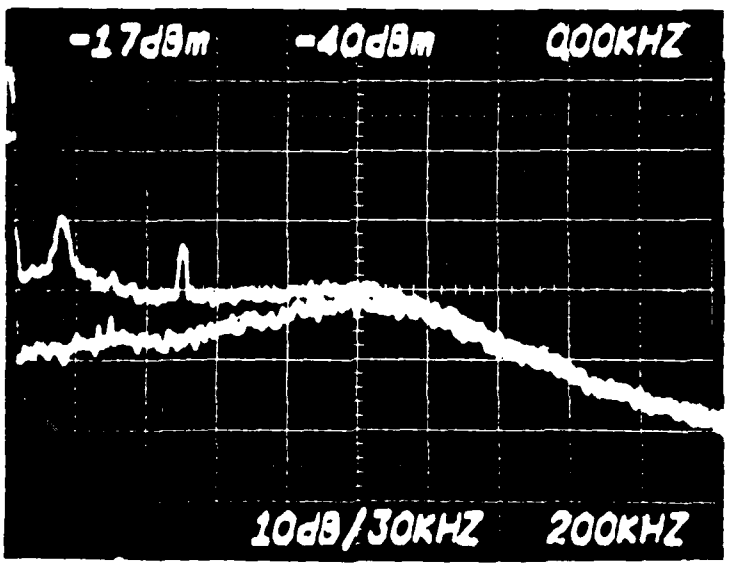

Fig. 6.3(d)
Top traces: Subtractor Output for two modulation levels with the interferometer stabilized.
Bottom traces: Subtractor output with apertures blocked. The rolloff at 1 MHz is due to the transimpedance amplifier frequency response.

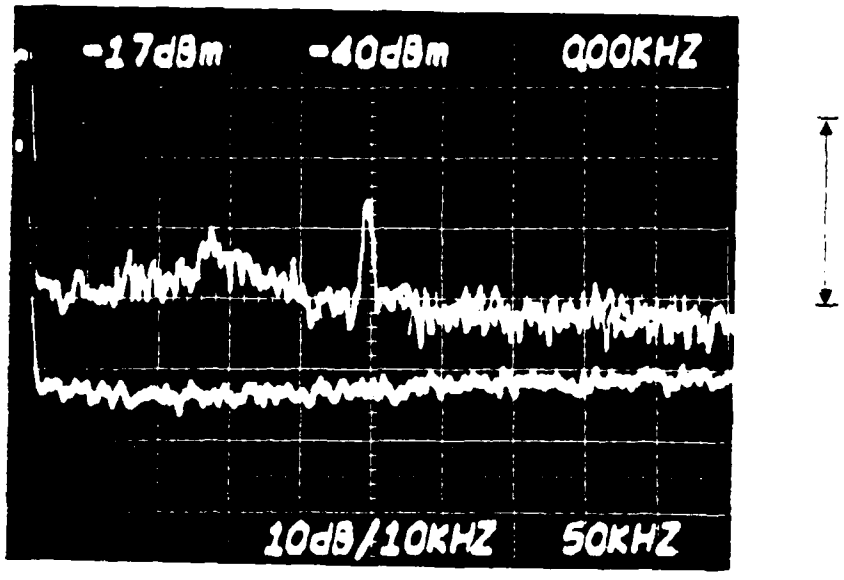

Fig. 6.3(e)
Unstabilized interferometer subtractor output with a modulation signal at f_m = 250 KHz. The arrow indicates the fluctuation range when the interferometer is not stabilized.

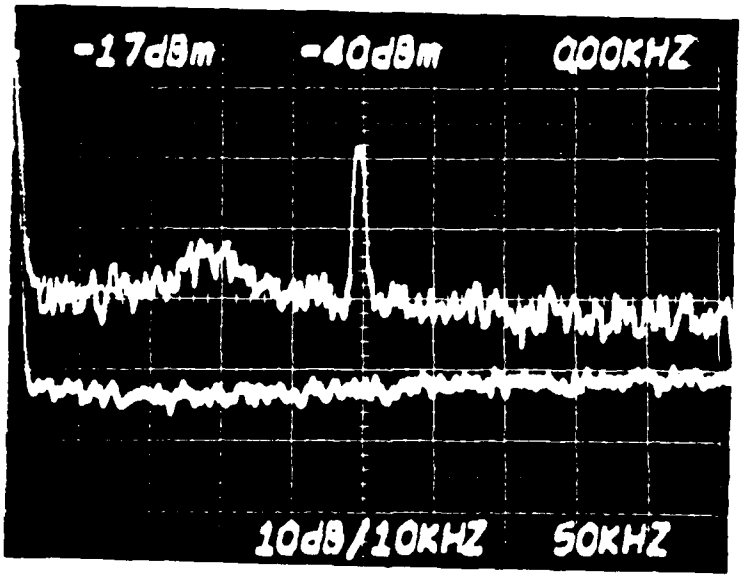

Fig. 6.3(f)
Top: Stabilized interferometer subtractor output with a modulation signal at f_m = 250 KHz.
Bottom: Subtractor output with both detectors blocked.

CHAPTER 7

CONCLUSIONS

The feedback stabilization scheme stabilized the interferometer output to a level which allowed the detection of a signal at the quantum limit of photodetection. The RMS noise reduction of 23 dB was sufficient to achieve the quantum limit of detection in a noisy environment.

The effect of laser source fluctuations was minimized by using two detectors in a balanced mixer configuration to suppress the excess noise. Mode drifting was not a problem when the detector bandwidth was much less than the mode separation. Polarization noise was minimized by orienting the input polarizer axis at 45 degrees to the two mode polarizations. This ensured that the transmitted intensity remained constant as the individual mode intensities varied.

A low noise amplifier was essential to ensure that amplifier thermal noise did not dominate shot noise for a low power laser. A transimpedance amplifier was designed and built for this purpose.

The bandwidth of the feedback loop was constrained by the integrator, which has a rolloff of 20 dB per decade. Since the noise spectrum was dominant at frequencies below 1 KHz, the integrator frequency response did not compromise the stabilization.

A PZT, instead of an EOM, was used as the feedback transducer because the correction factor introduced by the

EOM was wavelength dependent. A proposed scheme was to use a He-Ne laser for stabilization of the interferometer and a dye laser for the signal carrier. Thus the interferometer would be stable for the He-Ne beam but the signal beam would not be equally compensated. An alternative method was to use a single He-Ne laser beam by locking onto one polarization for stabilization and modulating the orthogonal component for the signal. Attempts to do this resulted in a weak signal beam to lock onto causing a poor stabilization of the interferometer. An experimental difficulty that was encountered was the limited bandwidth of the PZT/mirror. The system would oscillate at 600 Hz whenever feedback was applied. The problem was traced to the mechanical resonance of the PZT/mirror. Reducing the mass of the mirror eliminated the instability.

Application of the feedback stabilization scheme to the homodyne modulation experiment eliminated the fluctuations observed on the signal of the unstabilized interferometer. The noise on the stabilized signal was verified to be the quantum shot noise by comparing it with the shot noise generated by an equal intensity white light source. The measured noise for the stabilized signal and white light source was 0.96 μV and 0.97 μV, respectively, for transimpedance amplifier output voltages of V1 = 1.1 V and V2 = 1.0 V. This was measured at a frequency of 500 KHz with a lock-in amplifier time constant of 10 ms. The predicted

shot noise level was 0.92 μV. The discrepancy could be due to the component tolerance of R_f, the transimpedance gain. A nominal value of 100 K was used in Eq. (6.17) to calculate the theoretical shot noise level. Another factor which could contribute to the discrepancy is the accuracy of the value used for the noise equivalent bandwidth in Eq. (6.17), which was specified as $1/4\tau$ in the lock-in amplifier manual.

The feedback scheme has been successfully demonstrated in reducing the noise on a ring cavity used in the squeezed state generation of light. The feedback stabilization scheme will be applied to future experiments used in the generation of squeezed state light.

BURR-BROWN®

OPA101
OPA102

Low Noise - Wideband
PRECISION JFET INPUT OPERATIONAL AMPLIFIER

FEATURES

- GUARANTEED NOISE SPECTRAL DENSITY - 100% Tested
- LOW VOLTAGE NOISE - 8nV/$\sqrt{Hz}$ max at 10kHz
- LOW VOLTAGE DRIFT - 5μV/°C max (B grade)
- LOW OFFSET VOLTAGE - 250μV max (B grade)
- LOW BIAS CURRENTS - 10pA max at 25°C Ambient (B Grade)
- HIGH SPEED - 10V/μsec min (OPA102)
- GAIN BANDWIDTH PRODUCT - 40MHz (OPA102)

APPLICATIONS

- LOW NOISE SIGNAL CONDITIONING
- LIGHT MEASURMENTS
- RADIATION MEASUREMENTS
- PIN DIODE APPLICATIONS
- DENSITOMETERS
- PHOTODIODE/PHOTOMULTIPLIER CIRCUITS
- LOW NOISE DATA ACQUISITION

DESCRIPTION

The OPA101 and OPA102 are the first FET operational amplifiers available with noise characteristics (voltage spectral density) guaranteed and 100% tested.

The amplifiers have a complementary set of specifications permitting low errors in signal conditioning applications: low noise, low bias current, high open-loop gain, high common-mode rejection, low offset voltage, low offset voltage drift, etc.

In addition, the amplifiers have moderately high speed. The OPA101 is compensated for unity gain stability and has a slew rate of 5V μsec. min. The OPA102 is compensated for gains of 3V V and above and has a slew rate of 10V μsec. min.

Each unit is laser-trimmed for low offset voltage and low offset voltage drift versus temperature. Bias currents are specified with the units fully warmed up at +25°C ambient temperature.

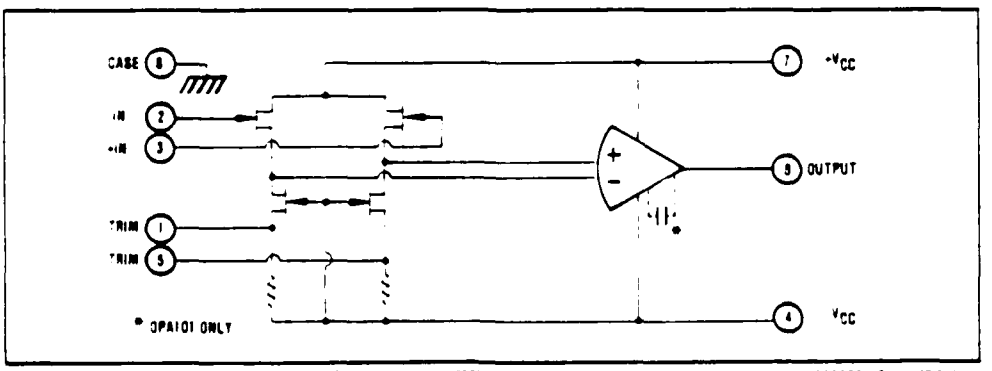

International Airport Industrial Park P.O. Box 11400 Tucson Arizona 85734 Tel: (602) 746-1111 Twx: 910-952-1111 Cable: BBRCORP Telex: 66-6491

PDS-414A

TYPICAL PERFORMANCE CURVES

T_A = +25°C, ±Vcc = ±15VDC unless otherwise noted. Performance curves apply to both OPA101 and OPA102 unless otherwise noted.

INPUT NOISE VOLTAGE VS FREQUENCY

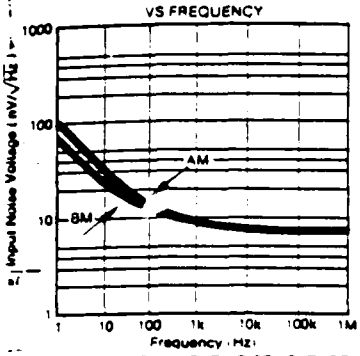

TOTAL INPUT NOISE VOLTAGE VS FREQUENCY

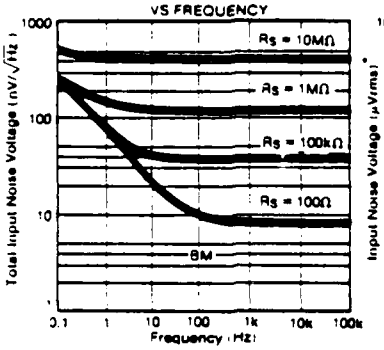

RMS INPUT NOISE VOLTAGE VS SOURCE RESISTANCE

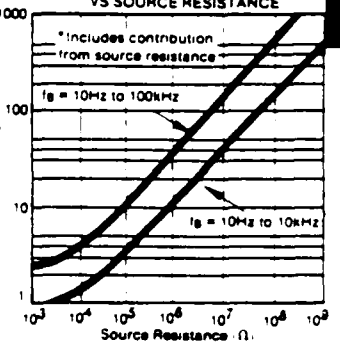

PEAK-TO-PEAK INPUT NOISE VOLTAGE VS SOURCE RESISTANCE

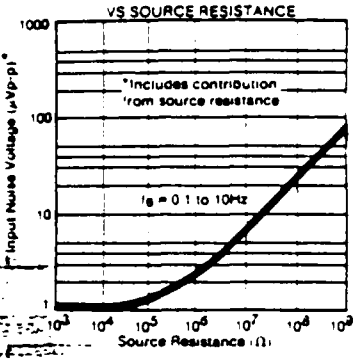

INPUT NOISE CURRENT VS FREQUENCY

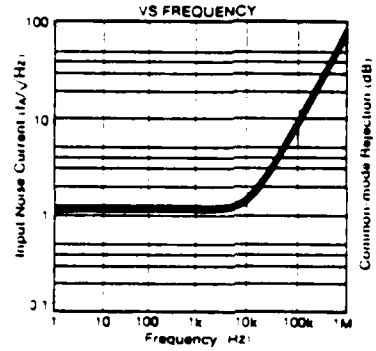

COMMON-MODE REJECTION VS FREQUENCY

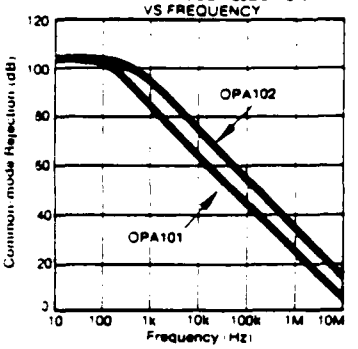

OPEN-LOOP FREQUENCY RESPONSE

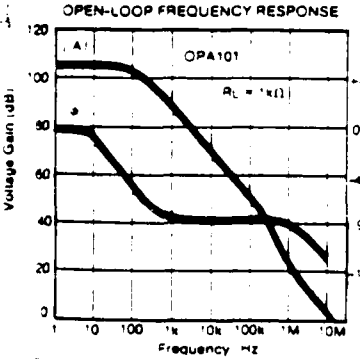

LARGE SIGNAL TRANSIENT RESPONSE

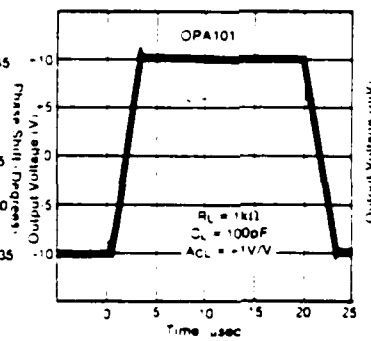

SMALL SIGNAL TRANSIENT RESPONSE

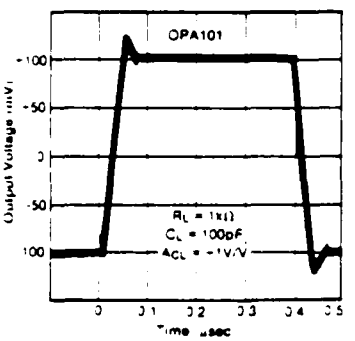

OPEN-LOOP FREQUENCY RESPONSE

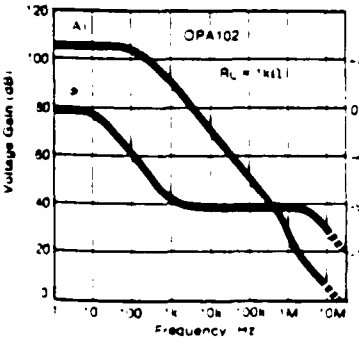

LARGE SIGNAL TRANSIENT RESPONSE

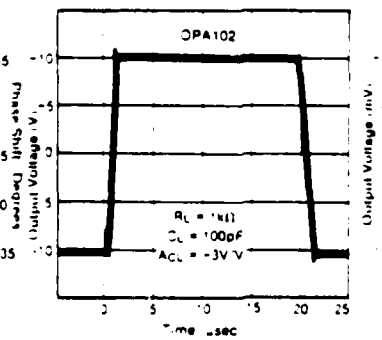

SMALL SIGNAL TRANSIENT RESPONSE

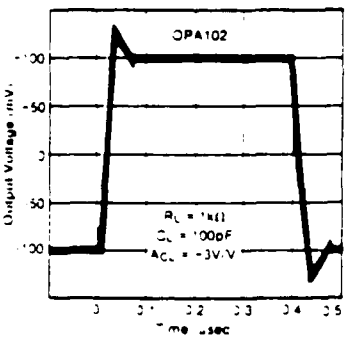

REFERENCES

1. Maeda, M., Ph.D. Research, Research Laboratory of Electronics, MIT, 1984.

2. Haus, H.A., Waves and Fields in Optoelectronics, Prentice-Hall, 1984.

3. Smith, R.G., Personick, S.D., "Receiver Design for Optical Fiber Communication Systems", Topics in Applied Physics, Vol. 39, Semiconductor Devices for Optical Communication, Springer Verlag, 1982.

4. Keiser, G., Optical Fiber Communications, McGraw Hill, 1983.

5. Gowar, J., Optical Communication Systems, Prentice Hall, 1984.

6. Ott, H., Noise Reduction Techniques in Electronic Systems, J. Wiley and Sons, 1976.

7. Kennedy, R., "Communication Through Optical Scattering Channels: An Introduction," Proc. IEEE, Vol. 58, 1970, p. 1651.

END

FILMED

8-85

DTIC